The Meteoritical Society

Meteoritics & Planetary Science 55, Nr 8, 1764–1792 (2020)
doi: 10.1111/maps.13546

Sierra Gorda 009: A new member of the metal-rich G chondrites grouplet

Marina A. IVANOVA*[1], Cyril A. LORENZ[1], Munir HUMAYUN[2], Catherine M. CORRIGAN[3], Thomas LUDWIG[4], Mario TRIELOFF[4], Kevin RIGHTER[6], Ian A. FRANCHI[5], Alexander B. VERCHOVSKY[5], Ekaterina V. KOROCHANTSEVA[1], Vladimir V. KOZLOV[7], Svetlana N. TEPLYAKOVA[1], Alexander V. KOROCHANTSEV[1], and Victor I. GROKHOVSKY[8]

[1]Vernadsky Institute of Geochemistry and Analytical Chemistry, Moscow 119991, Russia
[2]National High Magnetic Field Laboratory and Department of Earth, Ocean & Atmospheric Science, Florida State University, 1800 E. Paul Dirac Drive, Tallahassee, Florida 32310, USA
[3]National Museum of Natural History, Smithsonian Institution, Washington, District of Columbia 20560, USA
[4]Institut für Geowissenschaften, Klaus Tschira-Labor für Kosmochemie, Ruprecht-Karls-Universität Heidelberg, D-69120 Heidelberg, Germany
[5]Planetary and Space Sciences Research Institute, Open University, Milton Keynes MK7 6AA, UK
[6]NASA – Johnston Space Center, Mailcode XI2, Houston, Texas 77058, USA
[7]Oxford Instruments OM & Gatan Inc, Moscow Office 26, Denisovskii Pereulok, Moscow 105005, Russia
[8]Ural Federal University, Ekaterinburg 620002, Russian Federation
*Corresponding author. E-mail: meteorite2000@mail.ru; ivanovama@si.edu

(Received 20 January 2020; revision accepted 05 July 2020)

Abstract–We investigated the metal-rich chondrite Sierra Gorda (SG) 009, a member of the new G chondrite grouplet (also including NWA 5492, GRO 95551). G chondrites contain 23% metal, very reduced silicates, and rare oxidized mineral phases (Mg-chromite, FeO-rich pyroxene). G chondrites are not related to CH-CB chondrites, based on bulk O, C, and N isotopic compositions, mineralogy, and geochemistry. G chondrites have no fine-grained matrix or matrix lumps enclosing hydrated material typical for CH-CB chondrites. G chondrites' average metal compositions are similar to H chondrites. Siderophile and lithophile geochemistry indicates sulfidization and fractionation of the SG 009 metal and silicates, unlike NWA 5492 and GRO 95551. The G chondrites have average O isotopic compositions $\Delta^{17}O>0‰$ ranging between bulk enstatite (E) and ordinary (O) chondrites. An Al-rich chondrule from SG 009 has $\Delta^{17}O>0‰$ indicating some heterogeneity in oxygen isotopic composition of G chondrite components. SG 009's bulk carbon and nitrogen isotopic compositions correspond to E and O chondrites. Neon isotopic composition reflects a mixture of cosmogenic and solar components, and cosmic ray exposure age of SG 009 is typical for O, E, and R chondrites. G chondrites are closely related to O, E, and R chondrites and may represent a unique metal-rich parent asteroid containing primitive and fractionated material from the inner solar system. Oxidizing and reducing conditions during SG 009 formation may be connected with a chemical microenvironment and possibly could indicate that G chondrites may have formed by a planetesimal collision resulting in the lack of matrix.

INTRODUCTION

The study of metal-rich meteorites with textural similarities to CH or CB chondrites from different solar system reservoirs and/or locations may provide a better understanding of early chemical fractionation processes in the solar system, formation and accretion of metal-rich parent bodies, and relationship to other types of material. The metal-rich chondrites (~20 vol% of Fe,Ni-metal) are very intriguing meteorites and have attracted a lot of attention recently. They include carbonaceous (C) chondrites—CH, CBa + CBb chondrites (Weisberg

[Correction added on 02 September 2020 after first online publication: Table 2 column NWA 5492 data is amended.]

et al. 1990, 2001; Meibom et al. 1999; Campbell et al. 2001; Krot et al. 2002, Ivanova and Petaev 2015), the CH/CBb chondrite Isheyevo (Ivanova et al. 2008), the recently studied metal-rich chondrites Northwest Africa (NWA) 5492 and Grosvenor Mountains (GRO) 95551 (Weisberg et al. 2012, 2015), and new ungrouped chondrites NWA 12273 and 12379 which have affinities to L/LL chondrites (Agee et al. 2019; Jansen et al. 2019).

CB chondrites (bencubbinites) are divided into CB_a (coarse-grained) and CB_b (fine-grained; Weisberg et al. 2001). They consist of chemically zoned (CB_b) and unzoned (CB_a) Fe,Ni-alloy, non-porphyritic (skeletal olivine, SO), and cryptocrystalline (CC) magnesian chondrules, which predominate over other clast types. Chondrules have a narrow range of oxygen isotopic compositions ($\Delta^{17}O \sim -2.5 \pm 0.5‰$), while refractory inclusions surrounded by a Wark–Lovering rim are depleted in ^{16}O ($\Delta^{17}O \sim$ from $-15‰$ to $-5‰$) compared to CV3 CAIs. CB chondrites contain hydrated lithic clasts, and lack the matrix component (Weisberg et al. 2001; Krot et al. 2014, 2017). Despite a lot of data, the origin of CB chondrites remains unclear. Whether their chondrules and other components formed in the early solar nebula (Newsom and Drake 1979; Weisberg et al. 1990, 2001; Meibom et al. 1999; Campbell et al. 2001; Krot et al. 2002) or are products of late stage protoplanetary collisions (e.g., Wasson and Kallemyn 1990; Campbell et al. 2002, 2005; Amelin and Krot 2005; Krot et al. 2005; Fedkin et al. 2015; Oulton et al. 2016), remains debatable.

CH chondrites mainly consist of zoned and unzoned Fe,Ni-metal (22 vol%) and common carbonaceous chondrite chondrules—magnesian, ferrous, and Al-rich porphyritic chondrules, the oxygen isotopic compositions of which vary over a wide range ($\Delta^{17}O$ ~from $-5‰$ to $+4‰$). Like CB chondrites, CH chondrites do not have a matrix component. Refractory inclusions are surrounded by Wark–Lovering rims, which have $\Delta^{17}O \sim -24‰$ (Kimura et al. 1993; Weber et al. 1995; Ivanova et al. 2008; Krot et al. 2008, 2010, 2012). Krot et al. (2008, 2010, 2012) suggested that CB and CH chondrites are genetically related and represent different samples of chondritic components formed by both shock and nebular processes. Weisberg et al. (1995b) also pointed out the chemical and isotopic similarities of CB, CH, and CR chondrites and proposed combining them into a single CR clan of meteorites. According to this work, the CR clan meteorites formed at the same time and at approximately the same heliocentric distance.

The Isheyevo meteorite (CH/CBb) has the characteristics of both CH and CB chondrites (Ivanova et al. 2008). It is known that CH/CBb chondrites have the heaviest nitrogen ($\delta^{15}N > 1000‰$; Sugiura et al. 2000; Weisberg et al. 2001), like all other CB chondrites, and carbon is enriched in the heavy isotope. Isheyevo has a K-Ar age 3.4 Ga, but it cannot be ruled out that shock events affected this age. The cosmic ray exposure (CRE) age, determined by cosmogenic ^{38}Ar, is 34 Ma, which corresponds to the age of the bencubbinites of the CBa group (Ivanova et al. 2008).

Two recently studied ungrouped meteorites, NWA 5492 and GRO 95551 (Weisberg et al. 2012, 2015), have affinities to CH-CB chondrites, but their silicate compositions are more reduced than those in CH and CB chondrites. Sulfides in NWA 5492 and GRO 95551 are more abundant and not related to the metal, as in the CB chondrites. Average metal compositions in NWA 5492 and GRO 95551 are close to H chondrite metal. Oxygen isotopic compositions of NWA 5492 and GRO 95551 chondrules and their fragments show a range with most having $\Delta^{17}O$ values $>0‰$. Since there is no matrix component, their average chondrule + fragment oxygen isotopic compositions are considered to be representative of whole rock and ($\Delta^{17}O$ values) are between those for enstatite (E) and ordinary (O) chondrites. These data argue for a close relationship between NWA 5492 and GRO 95551 and suggest that they are the first examples of a new type of metal-rich chondrite, called G-chondrites (GCs; Weisberg et al. 2015).

NWA 12379 and 12273 (Agee et al. 2019; Jansen et al. 2019) are recently studied metal-rich chondrites with unique characteristics that distinguish them from meteorites of any previously described chondrite groups. They are listed as "probably paired" in the Meteoritical Bulletin. Silicates in these meteorites are similar to mildly metamorphosed L3 chondrites (Jansen et al. 2019). However, the high metal content (~70 vol%) and complete lack of matrix are inconsistent with OC classification; these characteristics are typical for metal-rich carbonaceous (CH and CB) and G chondrites. In contrast to the metal-rich chondrites, but similar to OCs, the meteorite NWA 12379 experienced thermal metamorphism that resulted in nearly complete chemical equilibration of chondrule olivine, and formation of Cl-apatite, merrillite, chromite, tetrataenite, and ferroan olivine that replaces low-Ca pyroxene. It is unclear whether the major components of this meteorite, chondrules and metal originate from the same cosmochemical reservoir in the early solar system or formed separately and were mixed together afterward.

The recent discovery of a possible new member of the G chondrites, Sierra Gorda (SG) 009, led us to perform a comprehensive petrologic, geochemical, and isotopic study of this meteorite (Ivanova et al. 2019). A goal of this investigation is to study the main properties

of a new grouplet of metal-rich GCs, and to discuss the possible origin of their components based on our comprehensive study of the SG 009 ungrouped metal-rich chondrite.

ANALYTICAL PROCEDURES

Mineralogy and Petrology

Two polished thin and thick sections with total surface area of ~5.5 cm^2 of the SG 009 meteorite were studied by optical microscopy at the Vernadsky Institute (Russia) and Ural Federal University (Russia). Backscattered electron (BSE) imaging and energy dispersive X-ray spectroscopy (EDS) analyses were performed using Tescan scanning electron microscope (SEM) with analytical equipment of the Oxford Instruments AztecLive Automate with detector UltimMax 100 (Russia) and FEI Nova NanoSEM 600 SEM the Smithsonian Institution (SI; USA). FEI Nova NanoSEM 600 SEM is equipped with a Thermo Electron energy dispersive X-ray spectrometer and the Noran System Six software at the SI. The SEM was operated at 15 kV with a beam current of 2–3 nA. Approximately half of the section was subsequently mapped in Si, Mg, Fe, Ca, Al, Ti, Fe, Ni, S, Cr, P X-rays using the FEI Nova NanoSEM 600. For both instruments, a fully focused electron beam was operated at 15 kV accelerating voltage, 100 nA beam current, 20–30 ms per pixel acquisition time, and a spatial resolution of ~2–3 μm per pixel. Ca, Al, Mg, Ti, Na, Cl, Fe, Ni, and Sc were measured using Kα lines. The elemental maps in Mg, Ca, and Al Kα were combined using an RGB-color scheme (Mg—red, Ca—green, Al—blue) and the ENVI (Environment for Visualizing Images) software package.

Mineral compositions were analyzed with a JEOL JXA-8530 + Hyperprobe five-spectrometer electron microprobe at the Smithsonian Institution. Operating conditions were 15 kV accelerating voltage, a fully focused beam with 20 nA beam current, and peak counting times of 20 s for major elements and 40 s for minor elements. Natural and synthetic minerals were used both as calibration standards and, in some cases, as unknowns that were analyzed at the beginning and the end of every run. Matrix corrections were applied using Phi-Rho-Z (for JEOL JXA 8530+) software routines. Detection limits for silicates were (wt%): SiO_2, TiO_2, Al_2O_3, Cr_2O_3, FeO, MnO, MgO, CaO, NiO—0.02; K_2O, Na_2O, Sc_2O_3, V_2O_3—0.05; ZrO_2—0.1; Y_2O_3—0.3; HfO_2—0.4. The modal abundances were estimated based on high resolution BSE images using Adobe Photoshop™ software. Platinum group elements (PGE) in metal particle of SG 009 were studied using a Tescan SEM with analytical equipment of the Oxford Instruments AztecLive Automate with detector UltimMax 100 (Russia) and a Tescan MIRA 3MLU SEM equipped with an INCA Energy 450 XMax 80 microanalysis system (Oxford Instruments Ltd.) at the V.S. Sobolev Institute of Geology and Mineralogy (IGM), Novosibirsk, Russia. EDS analyses of minerals were done in high-vacuum modes at an accelerating voltage of 20 kV, a probe current of 1 nA, and accumulation time of 20 s. The following simple compounds and metals were used as reference standards for most of the elements: SiO_2 (Si and O), Al_2O_3 (Al), diopside (Mg and Ca), $Ca_2P_2O_7$ (P), Cr_2O_3 (Cr), metallic Fe, Mn, Ni, Zn, Cu, and PGE. Correction for matrix effects was performed using the XPP algorithm, implemented in the software of the microanalysis system. Metallic Co served for quantitative optimization (normalization to probe current and energy calibration of the spectrometer).

Laser Ablation ICP-MS Analysis of Elemental Abundances

One section of SG 009 was analyzed using an Elemental Scientific Lasers New Wave™ UP193FX excimer laser ablation system coupled to a Thermo Element XR™, inductively coupled plasma mass spectrometer (LA-ICP-MS) at the Plasma Analytical Facility, Florida State University. Analyzed points are represented on Figs. S1a and S1 in supporting information. The oxide production was set with tuning the sample gas to yield ThO^+/Th^+ <1%. Metal and sulfide grains were measured with a 50 μm spot, at 50 Hz repetition rate, and 10 s of ablation per spot following Humayun (2012). Standards used were USGS silicate glasses GSC-1g, GSD-1g, and GSE-1g; NIST SRM 1263a steel; and the iron meteorites Hoba (IVB) and North Chile (Filomena, IIA). Silicate clasts were measured with either spot, line, or raster modes at 50 Hz repetition rate. Spots were taken with 100 μm spot size and 10 s of ablation per spot. Lines were taken with 50 μm spot size scanned at 10 μm s^{-1}. Rasters were taken with 100 μm spot size scanned at 20 or 25 μm s^{-1} covering areas of about 300 μm × 800 μm. Major and trace element concentrations for silicates were standardized with USGS silicate glasses GSC-1g, GSD-1g, BHVO-2g, BCR-2g, and BIR-1g (Humayun et al. 2010).

Oxygen, Neon, Argon, Nitrogen, and Carbon Isotopic Compositions

A separate split of the metal-rich lithology, weighing ~50 mg, was used to measure bulk oxygen, nitrogen, and carbon isotopic compositions at the Open

University. The sample was crushed in an agate mortar and pestle. Oxygen isotopic compositions were determined in replicate on ~2 mg aliquots of the partly homogenized sample by laser fluorination. The samples were heated with a CO_2 laser (10.6 nm) in the presence of excess BrF_5, the gas purified over hot KBr and cryogenic traps, and then analyzed on a PRISM III mass spectrometer (VG Isogas Ltd). Analytical precision is ~±0.8‰ and ±1.6‰ (2σ) for $\delta^{17}O$ and $\delta^{18}O$, respectively, providing a precision of ~±1.7‰ (2σ) for $\Delta^{17}O$. Details of the procedure are described by Miller et al. (1999).

Neon, argon, nitrogen, and carbon isotopic compositions were determined simultaneously using the Finesse mass spectrometer system, a complex of three static mode mass spectrometers fed from a single extraction system (Wright et al. 1988; Wright and Pillinger 1989; Verchovsky et al. 1998; Verchovsky 2017). The gases were extracted from the sample of SG 009 (13.44 mg) by stepped combustion in the temperature range from 200 to 1400 °C with 13 steps. The cleanup procedure of gases released by combustion and crushing methods was identical (Verchovsky et al. 1998, 2002). Typical system blank levels for stepped combustion were <10 ng of C and <1 ng of N. Typical system blanks for ^{20}Ne were $<6.5 \times 10^{-10}$, and for ^{40}Ar and ^{36}Ar were $<8 \times 10^{-9}$ and $<1.2 \times 10^{-10}$ (in cm^3 STP), respectively. The analytical precision is ~±1‰ for both $\delta^{13}C$ and $\delta^{15}N$ measurements. Uncertainties of absolute concentrations of gases are 5–10%, and elemental ratios of noble gases are estimated to have an uncertainty of about 5%.

SIMS Investigations of Oxygen Isotopes

Oxygen isotope compositions in olivine, pyroxene, and spinel were determined using the Cameca IMS1280-HR ion microprobe at Heidelberg University (HIP). We used a 2 nA, 20 keV Cs^+ primary ion beam with a raster size of 10 μm (12 μm during pre-sputtering). Negative secondary ions were accelerated to 10 keV. The secondary ion image was limited to 30 μm, the dynamic transfer optical system (DTOS) was activated, and sample charging was compensated with the electron gun (NEG). ^{16}O, ^{17}O, and ^{18}O were detected simultaneously in three Faraday cups. The nominal mass resolving power for ^{16}O and ^{18}O was 2500 and 7000 for ^{17}O. The contribution of $^{16}OH^-$ on the ^{17}O peak was negligible at <0.1‰. Secondary intensities for ^{16}O and ^{17}O were $\sim 1.5 \times 10^9$ cps and $\sim 6 \times 10^5$ cps, respectively. Prior to each analysis, the secondary beam was centered automatically in the field aperture (X and Y) and the entrance slit (X only). Including the time for beam centering, the analyses started after a total pre-sputtering time of 90 s and each analysis had 20 cycles with 10 s integration time per cycle. The internal precision reported is the standard deviation of the mean value of the isotope ratios. The baseline of the FC amplifiers was determined with an integration time of 300 s at least three times per session.

San Carlos olivine (+2.69, +5.28), pyroxene (+3.09, +6.03), and Burma spinel (+14.77, +28.09) were used as reference materials for calibration of the ol, px, and sp analyses (values in parentheses are $\delta^{17}O$ and $\delta^{18}O$ determined by laser fluorination mass spectrometry). The reference minerals were on a separate sample holder and were analyzed prior to and after each of the two analytical sessions. The external repeatability (1σ) for $\delta^{17}O$, $\delta^{18}O$, and $\Delta^{17}O$ of these analyses was 0.4, 0.5, and 0.3 for ol; 0.4, 0.3, and 0.4 for px; and 0.3, 0.7, and 0.4 for sp, respectively.

After the SIMS analyses, reflected light images of the regions analyzed were overlain with EDX element mappings to check for mixed phase analyses and reject them (see Fig. S2 in supporting information).

RESULTS

Petrography and Mineralogy

The SG 009 meteorite consists of a silicate fraction represented by chondrules and their fragments, and Fe, Ni-metal nodules (23 vol%; Fig. 1). The silicate fraction also includes 1 cm sized lithic fragments, some of which have an achondritic texture.

Chondrules in SG 009 are commonly 400 to 1.2 mm in size (Figs. 2a–d). Some angular chondrule fragments are up to 2 mm in size. The silicate fraction is dominated by porphyritic chondrules—porphyritic olivine (PO) or porphyritic pyroxene porphyritic (PP) chondrules—and their fragments. Porphyritic olivine–pyroxene (POP; Fig. 2a), barred olivine (BO), radial pyroxene (RP), cryptocrystalline (C), glass-rich porphyritic, Al-rich (Fig. 2b), and SiO_2-rich chondrules (Fig. 2c) are less common (one to two chondrules of each type). Thus, most of the porphyritic chondrules are either dominantly olivine or pyroxene and there is a lack of the porphyritic olivine–pyroxene chondrules (POP) that dominate carbonaceous (Ebel et al. 2016) and ordinary chondrites (Gooding and Keil 1981; Kita et al. 2010). Several objects in SG 009 have chondrule textures but are now clasts with irregular outlines and no evidence of once being spherical.

Mineral modes of SG 009 are (vol%; Table 1): olivine—5; low-Ca pyroxene—40, Ca-pyroxene—4; glass (feldspathic)—10; silica—1; Fe,Ni-metal (kamacite)—23; sulfide (mostly troilite—9 (troilite: daubréelite = 5:1), schreibersite—3, magnesiochromite, anorthite, spinel,

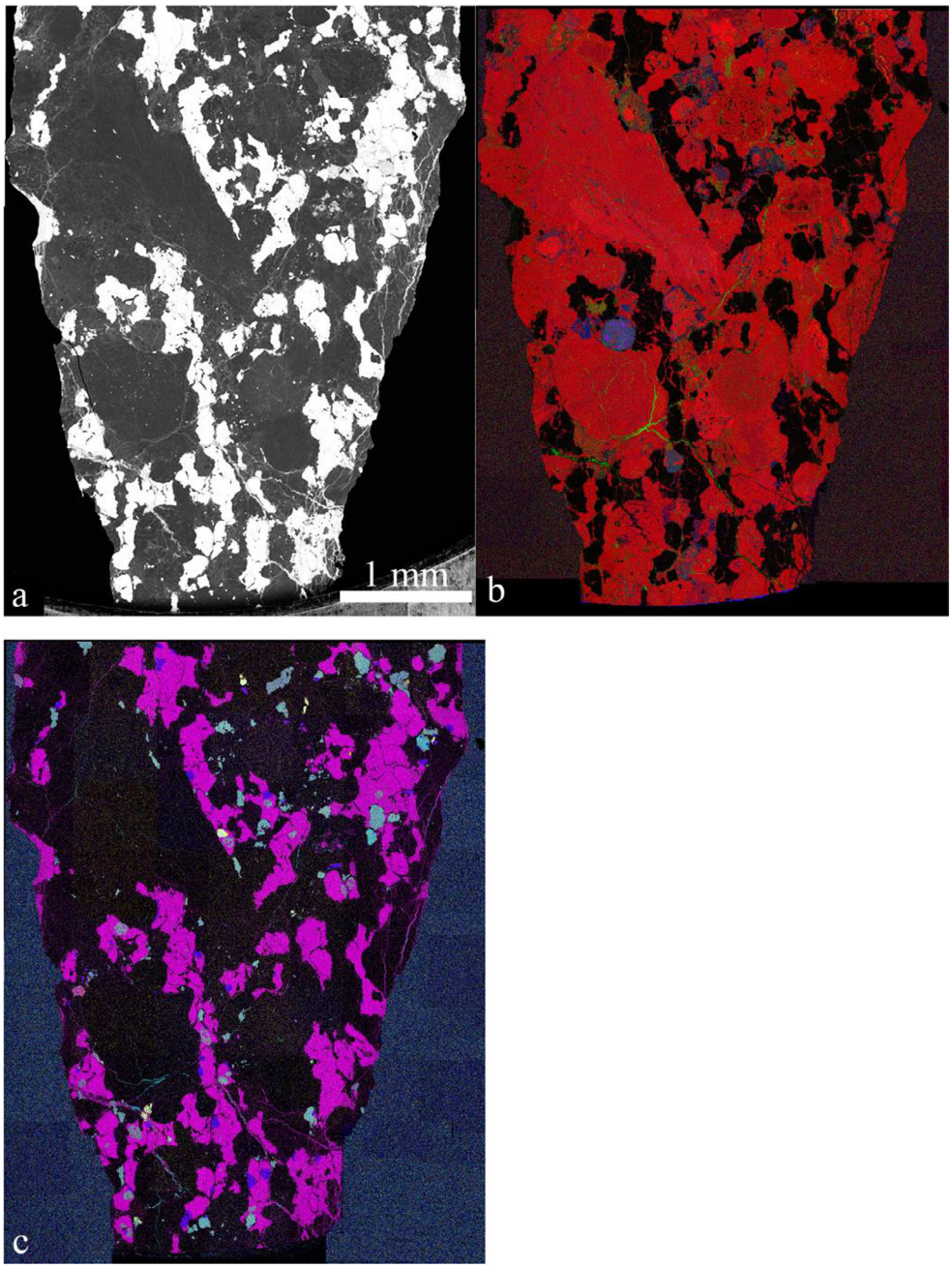

Fig. 1. Texture and constituents of Sierra Gorda 009. a) BSE image shows that the meteorite consists of a silicate fraction represented by chondrules and their fragments (dark gray), and Fe,Ni-metal nodules, 23 vol% (white). b) X-ray element map (Mg—red, Ca—green, Al—blue) shows chondrules and their fragments consisting of Mg-rich silicate (red), only one Al-rich chondrule occurs (blue). c) X-ray element map (Fe—pink, S—light blue, P—dark blue, Cr—yellow) shows that sulfide (light blue) is abundant, schreibersite (dark blue) and magnesiochromite (yellow) are rare. Scale bar is similar for all images.

graphite, and platinum group elements (PGE) metal particles <1, weathering products and fine-grained component ~5. Olivine abundance is lower than in ordinary chondrites. Mineral modes of SG 009 are mostly similar to those of NWA 5492 (Weisberg et al. 2012) with the exception of troilite which is more abundant in SG 009 (Fig. 1c), and magnesiochromite and (PGE)-metal particles rarely occurring in the meteorite.

Silicates in some chondrules contain tiny blebs of metal suggestive of reduction of Fe from silicates. One Al-rich chondrule (~500 μm in size) contains spinel,

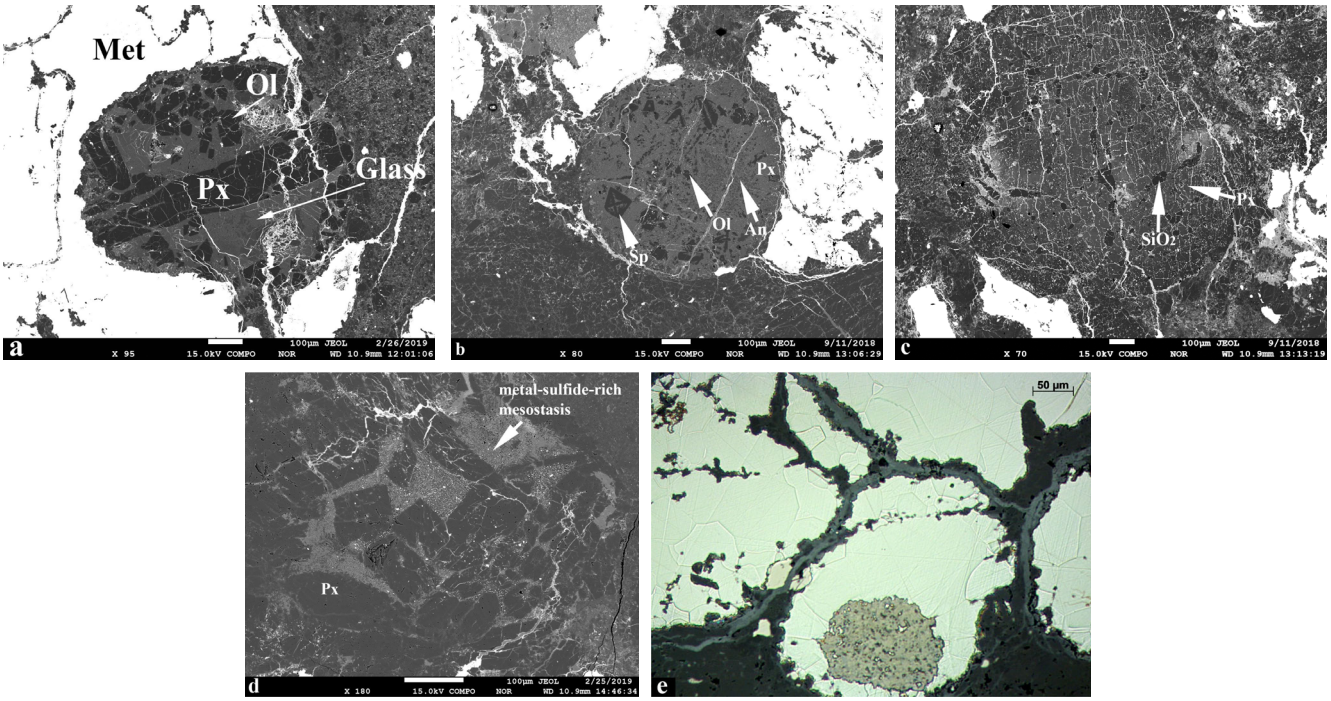

Fig. 2. BSE images of different objects from SG 009. (a) POP chondrule consisting of olivine (Ol), pyroxene (Px), and glassy mesostasis (glass), (b) Al-rich chondrule consisting of spinel (Sp), pyroxene, olivine, and anorthite (An), also shown on Fig. S2b—X-ray elemental map (Mg—red, Ca—green, Al—blue); (c) SiO_2-rich chondrules containing SiO_2—phase and pyroxene; (d) PP—chondrule consisting of pyroxene and metal-rich mesostasis; (e) etched grain of low-Ni metal with cross-cutting graphite grain in SG 009 (optical microscope, reflected light). (Color figure can be viewed at wileyonlinelibrary.com.)

Table 1. Modal abundances (vol%) of SG 009 compared to average metal-rich chondrites: NWA 5492, CH, CB, and NWA 12379 and ECs.

	SG 009	NWA 5492	EH3	EL3	CH	CB	NWA 12379
Olivine	5.2	6.3	4.4	2.4	–	–	–
Pyroxene	40.1	44.7	60.4	65.2	–	–	–
Ca-pyroxene	4.0	4.1	0.1	0.3	–	–	–
Glass	10.2	14.9	8.3	10.4	–	–	–
Silica	1.1	3.1	1.6	1.4	–	–	–
Fe-sulfide	9.2	2.5	10.4	7.6	<1	<1	5.0
Daubreelite	1.7	Trace	0.6	0.3	<1	<1	nf
Alabandite	<1	nf	nd	0.4	nf	nf	nf
Schreibersite	2.8	1.8	0.6	0.6	nf	nf	nf
Chromite	<1	nf	nf	nf	–	–	<1
Phosphate	nf	nf	nf	nf	nf	nf	<1
PGE particles	<1	nf	nf	nf	nf	nf	nf
Graphite	<1	nf	<1	<1	nf	nf	nf
FeNi	23.1	22.6	9.3	10.3	22.0	60–80	70.0

nf = not found, nd = not determined; NWA = Northwest Africa.
Data for NWA 5492, CH, and CB (Weisberg et al. 2001, 2015); data for NWA 12379 from Jansen et al. (2019).
Data for EH and EL from Weisberg et al. (1995a).

anorthite, and Al,Ti-rich diopside (Fig. 2b). It has an ideal round shape and clear boundaries with surrounding metal and silicate material. Silica-bearing chondrules (Fig. 2c) have irregular outlines, porphyritic texture, and consist of SiO_2-phase and pyroxene. Adjacent to spinel from an Al-rich chondrule, Mg-chromite was found in assemblage with daubréelite, troilite, and Fe,Ni-metal.

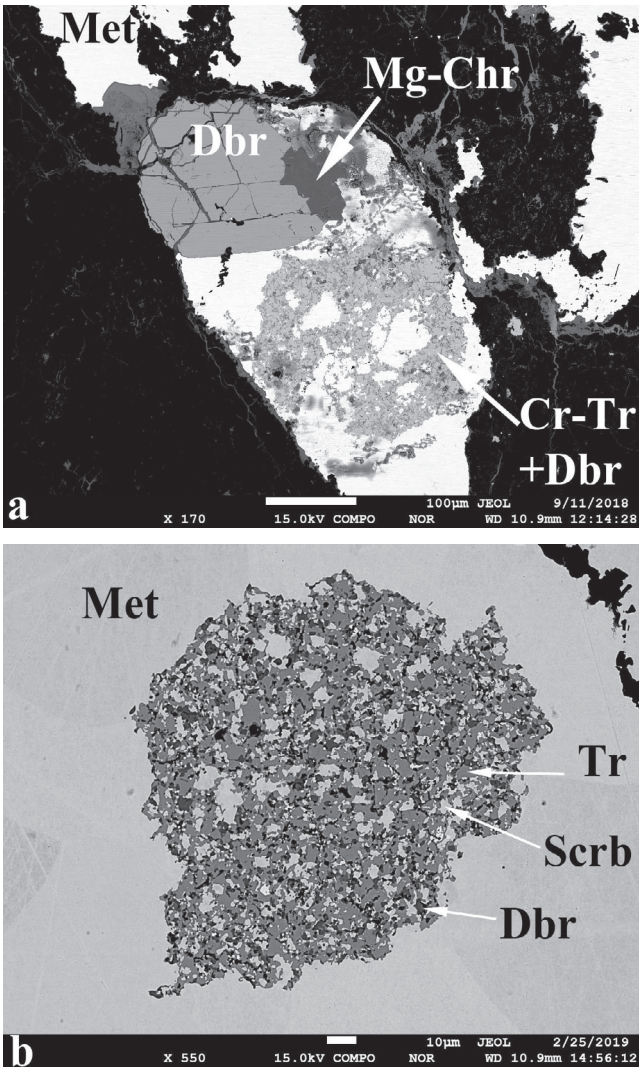

Fig. 3. BSE images of opaque assemblages from SG 009: (a) Fe,Ni-metal (Met)—daubreelite (Dbr)—Mg-chromite (Mg-Chr)—Cr-troilite (Cr-Tr) + daubreelite; (b) troilite+daubreelite+schreibersite (Scrb).

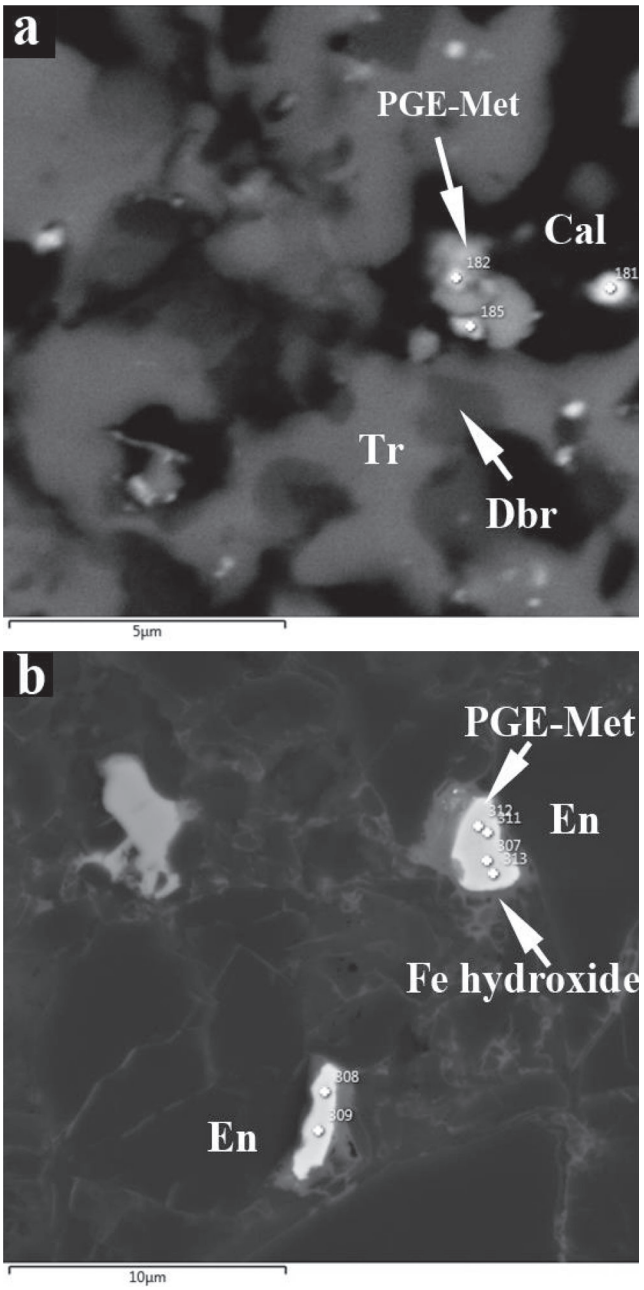

Fig. 4. PGE metal particles (PGE-Met) in: (a) troilite (Tr)–daubréelite assemblage surrounded by secondary calcite (Cal); (b) in enstatite (En) surrounded by iron hydroxide.

Opaque assemblages are represented by intergrown daubréelite, troilite, schreibersite, and Fe,Ni-metal (Figs. 3a and 3b). The Fe,Ni-metal in SG 009 occurs as ~600 μm diameter nodules or clusters of nodules, interstitial to the chondrules, or together with sulfides as the mesostasis of some chondrules (Fig. 2d). In one case, a graphite vein cuts through metal grains (Fig. 2e). After etching, kamacite demonstrates a polycrystalline structure (Fig. 2e) with equilibrium boundaries of grains that indicates long-duration recrystallization at temperatures above 500 °C. Tiny PGE-rich metal particles (up to 5 μm) were observed mostly in intergrowths with schreibersite–daubréelite–troilite assemblages surrounded by tiny secondary calcite grains and iron hydroxides, and in the silicate material (Figs. 4a and 4b).

While the metal abundance of SG 009 is similar to that of CH chondrites, the occurrence of large metal clasts is texturally similar to CB chondrites and to GRO 95551 (Weisberg et al. 2001).

One fragment of 1 cm length and 0.4 cm width has an elliptical shape and achondritic texture (Fig. 5). It is

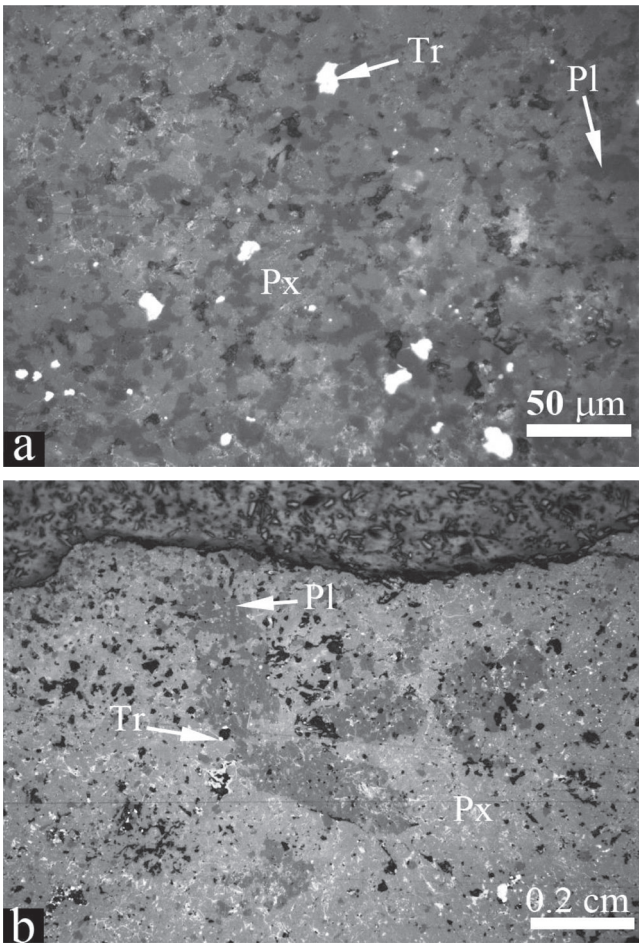

Fig. 5. a) Reflected light image of fine-grained area of achondritic clast (50×). Pyroxene is light gray, plagioclase is dark gray, troilite is white. b) Reflected light image of medium-grained area of achondritic clast (20×). Pyroxene is gray, plagioclase is dark gray, oxide is light gray, troilite is white.

composed of irregularly distributed areas of fine-grained and medium-grained texture. The fine-grained areas are composed of subhedral pyroxene crystals from 5 to 15 μm with interstitial anhedral feldspar grains of the same size. Medium-grained areas are composed mostly of 50–100 μm anhedral pyroxene with only minor 100 μm anhedral feldspar. Troilite is an accessory phase with grains of irregular shape and average 10 μm in size. The modal mineral composition (vol%) of the fine-grained area is: pyroxene 72.8; plagioclase 25.9; troilite 1.3; medium-grained areas: pyroxene 79.8; plagioclase 17.6; oxides 2.7.

The meteorite shock stage is S2 (Stoffler et al. 1991) based on undulatory extinction and the absence of planar fractures in olivine grains, corresponding to shock pressure <10 GPa.

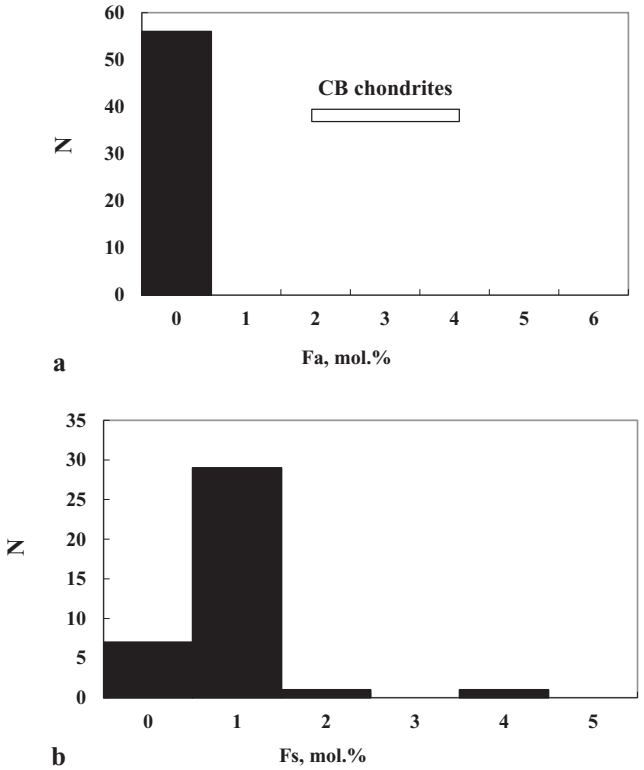

Fig. 6. Chemical compositions of (a) olivine compared to olivine composition of CB chondrites and (b) low-Ca-pyroxene in SG 009. N—number of grains.

Mineral Chemistry

Olivines and pyroxenes in SG 009 are highly reduced compared to the mineral assemblages of chondrules from carbonaceous or ordinary chondrites. The average composition of olivine ($Fa_{0.47 \pm 0.10}$) is similar to that of other G chondrites, NWA 5492 and GRO 95551. Olivine composition is also similar to ECs ($Fa_{0.4}$; Rubin 2010) more magnesian than olivine from CH-CB chondrites ($Fa_{2\text{-}4}$; Weisberg et al. 2001) and very different from more ferrous olivine from ungrouped metal-rich chondrites NWA 12379/12273 (Agee et al. 2019; Jansen et al. 2019). Its Cr_2O_3 and CaO contents are low like in NWA 5492 and GRO 95551 (Fig. 6; Table 2).

Average low-Ca pyroxene ($Fs_{1.42}$, $Wo_{0.88}$) with Fe/Mn ratio 2.83 is enstatite, the compositions of which are similar to those in other G chondrites, NWA 5492 and GRO 95551 (Weisberg et al. 2015), and ECs (Rubin 2010), and different from ungrouped metal-rich chondrites NWA 12379/12273 (Agee et al. 2019; Jansen et al. 2019; Table 3). Pyroxene is also represented by diopside ($Fs_{1.34}$, $Wo_{47.32}$). FeO-rich low-Ca-pyroxene occurs in some chondrules ($Fs_{9.33\text{-}32.48}$, $Wo_{0.23\text{-}4.74}$). Plagioclase varies in composition,

Table 2. Average composition of olivine (wt%) in SG 009, and other metal-rich chondrites, NWA 5492, GRO 95551, CH, CB and NWA 12379 chondrite.

	SG 009	NWA 5492	GRO 95551	Bencubbin	HaH 237	NWA 12379
SiO_2	42.7 ± 0.17	41.9	42.2	42.0	41.2	38.8
Cr_2O_3	0.04 ± 0.02	0.03	<0.1	0.6	0.5	0.1
FeO	0.51 ± 0.11	0.3	1.5	3.5	4.1	23.6
MnO	0.15 ± 0.02	0.1	0.2	0.2	<0.1	0.4
MgO	57.8 ± 0.19	57.3	55.4	54.1	53.0	38.8
CaO	0.04 ± 0.02	<0.1	<0.1	0.2	0.2	0.1
Total		99.6	99.3	100.6	99.0	101.8
Fa (mol%)	0.49 ± 0.11	0.3	1.3	3.4	4.1	25.4
SD		0.2	0.8	0.4	1.4	2.4
# grains	64	43	21	31	27	37

$An_{32.28\text{-}95.04}$. Mesostasis in chondrules is enriched in K_2O (3.83–9.18 wt%) and TiO_2 (1.22–6.53 wt%). MgO-chromite is almost pure MgO-endmember, $MgCr_2O_4$. Such chromite has not been described for any of the metal-rich chondrites before.

The one Al-rich chondrule (Figs. 2b and S2b) contains spinel, plagioclase, olivine, and pyroxene. Pyroxene is represented by diopside (Fs0.4-0.8, Wo47.1-50.2) enriched in Al_2O_3 (3.1–3.2 wt%) and TiO_2 (7.2–11.5 wt%). Spinel is enriched in Cr_2O_3 (3.52 wt%; Table 3), while plagioclase is almost pure anorthite (An98).

Pyroxene in the clast with achondritic texture (Fig. 5) is also very reduced ($En_{96.8\pm1.19}$ $Wo_{0.5\pm0.09}$), and minor pyroxene has composition: $En_{45.5\pm1.72}$ $Wo_{44.1\pm1.48}$. The low-Ca pyroxene contains Cr_2O_3 0.15 ± 0.04, Fe/Mn = 10.5 ± 7.3 (at.). The CaO-rich pyroxene is TiO_2-, Cr_2O_3-, and Na_2O-bearing (TiO_2 0.33 ± 0.03; Cr_2O_3 0.53 ± 0.09; Na_2O 0.41 ± 0.02 wt%). Feldspar composition is $Ab_{74.2}$ $An_{18.2}$ with 1.55 wt% FeO.

Metal in SG 009 is fairly uniform in composition. Average metal composition (wt%) is 4.99 ± 0.23 Ni, 0.44 ± 0.02 Co, and the metal contains less than 0.03 Si, P, and Cr. The high-Ni metal in SG 009 contains (wt%) 32.3 Ni and 0.25 Co. The low-Ni metal does not have solar Ni/Co ratio that is common in CH and CB chondrites. It is closer in composition to that of NWA 5492 than to GRO 95551 (Weisberg et al. 2012; Fig. 7).

Sulfides are represented by Cr-rich troilite (up to 2.4 wt%) and daubréelite that is enriched in Mn (up to 2.2 wt%; Table 4). We did not observe alabandite, which was reported by Friend et al. (2011) in the G-chondrite NWA 5492. Alabandite was described in E chondrites and in one inclusion from the Ghubara L chondrite (Ivanova et al. 2001). Schreibersite is homogeneous in composition.

Representative platinum group element (PGE)-enriched metal inclusion compositions are given in Table 5. PGE-enriched Fe,Ni-metal particles are mostly enriched in Pt, Ru, Os, and Ir. These particles have homogeneous (particle # 3, 46, and 1554) and heterogeneous (particles #31 and 4520) chemical compositions. As shown in Table 5, the average compositions of different particles vary in a wide range (particle #46 and 1554), as well as compositions inside particles (particles #31 and 4520). Contents of Pt, Os, Ir, and Ru in Fe,Ni-metal particles vary in a wide range (in wt%): Pt 1.79–27.6; Os 0.10–4.78; Ir 0.39–7.33; Ru 1.55–10.6; Pd up to 0.28. These compositions are distinct from those of fremdlinge observed in CAIs (e.g., Hewins et al. 2014) and of PGE particles found in R chondrites (Schulze 2007).

Siderophile and Chalcophile Element Geochemistry of Metal and Sulfides from SG 009

Results for 28 metal nodules and six sulfide grains from SG 009 analyzed by LA-ICP-MS are given in Tables 6 and 7 and shown in Fig. 8. Preliminary results were reported earlier in Ivanova et al. (2019). The locations of all analytical points are shown in the BSE image (Figs. S1a and S1b), and the numbers shown in the BSE image (Figs. S1a and S1b) correspond to those marked in Tables 6 and 7. The elements V (1 ppm), Cr (6 ppm), Mn (1 ppm), and Sb (0.2 ppm) were below detection limits in all but one metal nodule, 127-G, that had 23 ppm Cr and 1 ppm V. Neither Nb nor Ta was found in metal.

The average metal composition of the SG 009 metal is a good match to that of the metal in NWA 5492 and GRO 95511 and differs from average metal compositions of equilibrated H chondrite, CR, and CB_b chondrites (Fig. 8). One important difference is that the SG 009 metal has a wide range of compositions (e.g., an order of magnitude variation) among the compatible elements (Re, Os, Ir, Pt, Ru) compared to the metal of NWA 5492 G-chondrite, which exhibits a narrow range (±10%) in the compatible elements (Fig. 8).

Table 3. Average and representative analyses of pyroxene, plagioclase, glass, chromite, and spinel compositions (wt%) in SG 009.

	SiO_2	TiO_2	Al_2O_3	Cr_2O_3	FeO	MnO	MgO	CaO	Na_2O	K_2O	Total	Fs (mole%)	Wo (mole%)	An (mole%)	Ab (mole%)
Low-Ca-Px (39)	58.9 ± 0.7	0.1 ± 0.1	0.7 ± 0.6	0.3 ± 0.1	0.7 ± 0.2	0.3 ± 0.1	39.1 ± 0.7	0.5 ± 0.01	0.01 ± 0.0	0.02 ± 0.0	100.5	1.4 ± 0.4	0.9 ± 0.6		
FeO-rich low-Ca Px	56.9	b.d.	0.06	0.24	6.21	0.21	34.78	0.36	b.d.	b.d.	98.8	9.3	0.7		
FeO-rich low-Ca Px	52.0	0.10	1.62	0.51	20.18	0.41	23.08	1.31	b.d.	b.d.	99.2	32.5	2.6		
Ca-Px	55.4	0.00	2.11	0.00	1.07	b.d.	21.80	19.7	b.d.	b.d.	100.0	1.3	46.3		
Al-rich Ca-Px	51.3	0.65	12.5	0.63	1.23	0.06	31.48	3.21	b.d.	0.02	101.1	2.1	6.7		
Al-rich low-Ca-Px	49.7	0.41	15.4	0.50	1.22	0.08	31.76	1.56	b.d.	0.02	100.7	2.2	3.3		
Plagioclase	59.5	0.05	19.6	0.05	0.90	0.04	9.70	4.30	4.86	0.19	99.2			32.3	66.0
Plagioclase	51.5	0.05	31.3	0.02	1.03	0.02	0.23	12.6	3.64	0.10	100.6			65.4	34.0
Plagioclase	57.0	0.00	28.6	0.01	0.20	b.d.	0.19	9.32	6.38	0.13	101.8			44.4	54.9
Plagioclase	43.2	0.06	37.1	0.00	0.09	b.d.	0.02	18.1	0.80	0.04	99.5			92.4	7.4
Glass	65.3	0.02	22.9	0.02	0.54	0.02	0.49	2.66	8.47	0.37	100.8				
Glass	65.6	0.08	19.7	0.00	0.64	b.d.	0.11	0.82	4.29	9.18	100.5				
Glass	51.8	3.06	11.5	0.24	0.33	0.03	11.89	16.9	2.39	0.24	98.4				
Mg-chromite	b.d.	0.28	0.00	77.3	2.15	2.46	18.7	b.d.	b.d.	0.02	100.9				
Spinel	b.d.	0.04	67.93	3.53	0.29	0.09	28.34	0.04	b.d.	b.d.	100.3				

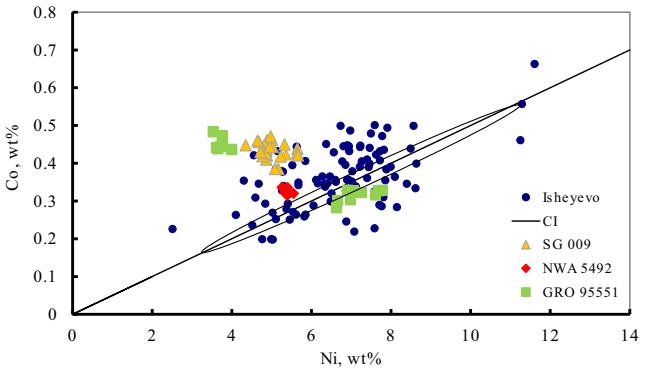

Fig. 7. Composition of metal in SG 009, NWA 5492, GRO 95551 (Weisberg et al. 2015), compared to metal from CBb chondrites (Campbell et al. 2001), Isheyevo CH/CBb (Ivanova et al. 2008) relatively CI (Anders and Grevesse 1989). (Color figure can be viewed at wileyonlinelibrary.com.)

The abundances of the volatile elements, Ga (16 ppm versus 15 ppm), Ge (26 ppm versus 26 ppm), Au (0.61 ppm versus 0.67 ppm), and Sn (0.4 ppm versus 0.5 ppm), overlap within analytical error between the metal of SG 009 and NWA 5492. Antimony abundances were below detection limits in NWA 5492 metal (<0.2 ppm) but consistent with the 0.12 ppm observed in SG 009 metal. Abundances for As (4.0 ppm versus 4.8 ppm) are also similar between the metals of the two chondrites. The Cu abundances differ more substantially (37 ppm versus 54 ppm). Other diagnostic features include the $(Ni/Co)_{CI}$ ratio that is identical between the two chondrites (0.75 versus 0.76) and lower than that of carbonaceous chondrites. The metal of the G chondrites is higher in volatile element abundances than that of CB or CR chondrites by an order of magnitude or more (Fig. 8).

In several sulfides from SG 009, strong enrichment of V, Cr, and Nb compared to CI compositions (Table 7) was observed in SG 009 (sulfides were not measured in NWA 5492). Vanadium is higher in the sulfides (500–1100 ppm) than in the silicates (<100 ppm). Similarly, Cr is higher in the sulfides (3–7 wt%) than in the silicates (0.05–0.5 wt%). Niobium contents in sulfides (~0.6 ppm) are higher than those in silicates of SG 009. Tantalum is generally lower in the sulfides (<0.002 ppm) with one exception, relative to the silicates (0.009–0.060 ppm).

Lithophile Element Geochemistry of Silicates in Chondrules from SG 009

All spots, lines, and rasters measurements taken on the silicate chondrules of SG 009 are shown in Figs. S1a and S1b. Rasters over the analyzed areas that were 400 μm or more in diameter are generally more representative of bulk compositions of the chondrule fragments than spot analyses, and results are represented in Table 7. Average data of the fragments correspond to a mixture of pyroxene, olivine, and plagioclase/glass compositions. The REE patterns have strong anomalies (Fig. 9). In addition to Eu anomalies, REEs show anomalies in Ce (all positive), that might be suspect for desert meteorites or might be cosmochemical in origin; in Yb, mainly positive, which is almost certainly a cosmochemical signal of volatilization in a reducing gas.

Other evidence for a reducing environment is provided by subchondritic Nb/Ta ratios in silicates, where Nb has acted like a chalcophile element. As mentioned above, sulfides have strong enrichments in V, Cr, and Nb compared to silicates (Table 7) corroborating the evidence of Nb depletion observed in the silicates. The complementary relationship between Nb in silicates and sulfides indicates that the metal, sulfide, and silicate clasts were all processed together in the same impact event. We observed strong fractionation of the Th/Sc ratio, immune to volatility, but sensitive to igneous processes, though there are no correlations between Sc and Sr or CaO and Al_2O_3 that might indicate that the Th/Sc variations are simple mixtures of pyroxene and feldspathic glass. Accordingly, it is suspected that the various silicate clasts might have igneous precursors, similar to what was observed by Oulton et al. (2016) in the study of Gujba silicate clasts. This would support our observation in the metals (see below).

Oxygen Isotopic Compositions of SG 009 and Its Minerals

Bulk oxygen isotopic composition of SG 009 silicates obtained at Open University (‰) is $\delta^{17}O$ 3.763, 3.736; $\delta^{18}O$ 6.263, 6.169; $\Delta^{17}O$ 0.506, 0.528‰ (Fig. 10). These values are different from CH/CB carbonaceous chondrites (e.g., Isheyevo [Ivanova et al. 2008]), but plot intermediate between ordinary and enstatite chondrites in the three oxygen isotope diagram (Fig. 10). The oxygen isotopic composition is on a line with other metal-rich chondrites NWA 5492 and GRO 95551, described by Weisberg et al. (2015), and very close to HH chondrite Burnwell (Russell et al. 1998). However, it is different from the very metal-rich chondrites NWA 12379/12273 oxygen compositions, whose silicates have affinities to L/LL chondrites.

Oxygen isotopic compositions of SG 009 minerals were also analyzed by ion probe at Heidelberg University. Figures S2a and S2b show the thin section areas where analyses were performed. These measurements comprised various olivine and pyroxene crystals, and spinel and olivine from a single Al-rich

Table 4. Representative analyses of troilite, daubreelite, schreibersite, and Fe,Ni-metal in SG 009 (wt%).

	Fe	Cr	Ni	Mn	S	P	Si	Co	Total
Troilite	59.5	2.40	0.02	0.10	36.7	b.d.	b.d.	0.08	98.8
Troilite	61.1	1.28	0.04	0.03	36.7	b.d.	b.d.	0.05	99.1
Schreibersite	51.5	0.02	32.57	0.00	0.03	15.46	b.d.	0.11	99.6
Daubreelite	18.9	34.6	0.04	1.25	44.4	b.d.	b.d.	0.03	99.3
Fe,Ni-metal	93.8	b.d.	5.97	0.01	b.d.	0.08	b.d.	0.44	100.3
Fe,Ni-metal	62.2	b.d.	36.27	0.00	b.d.	0.05	b.d.	0.21	98.7
Fe,Ni-metal	69.1	b.d.	29.69	0.00	b.d.	0.06	b.d.	0.26	99.2

b.d. = below detection.

Table 5. Representative and average compositions of PGE-enriched Fe,Ni-metal particles in SG 009 (wt%) obtained by EPMA (2, 3, 5) and EDS (other points) analyses.

Area	N	Fe	Co	Ni	Ru	Rh	Pd	Os	Ir	Pt	Total
3	2	60.7	0.38	30.3	2.1	0.53	b.d.	1.6	0.93	1.79	98.36
	3	61.3	0.31	29.6	2.01	0.44	b.d.	1.65	0.83	2.12	98.29
	5	61.7	0.25	29.8	2.11	0.48	b.d.	1.44	1.16	2.08	99.03
31	181	53.0	0.32	6.52	1.55	0.28	b.d.	3.44	7.33	27.6	100
	182	52.6	0.41	22.3	2.07	b.d.	b.d.	0.91	4.19	17.5	100
	185	56.3	0.32	15.8	1.57	0.20	b.d.	2.28	5.35	18.1	100
4520	1	57.9	n.d.	18.1	3.17	0.30	0.27	4.78	5.91	9.63	100
	2	69.7	n.d.	20.7	2.11	0.20	0.17	1.69	2.07	3.32	100
46	Average (4)	67.7	0.46	17.4	7.94	1.52	0.28	0.10	0.39	4.22	100
	Average (2)	62.3	0.40	16.9	10.6	1.91	0.27	0.38	0.57	6.69	100
1554	Average (10)	61.1	0.36	30.1	2.30	0.52	b.d.	1.61	1.44	2.59	100

n.d. = not determined; b.d. = below detection limit.

chondrule (Fig. S2c). Results are presented in Table 8 and Fig. 11.

The majority of oxygen isotopic composition data of individual SG 009 minerals are similar to the two other GCs NWA 5492 and GRO 95551 as represented by mean values of olivine and pyroxene of ion probe data by Weisberg et al. (2012, 2015) in Fig. 11, and representative of the bulk oxygen isotopic composition of G chondrites (Fig. 10). However, individual spinel and olivine from the Al-rich chondrule display values below the terrestrial fractionation line indicating the same heterogeneity of oxygen isotopic compositions as found by Weisberg et al. (2012) for barred silicate clasts (Fig. 10) and Weisberg et al. (2015) for olivine in another Al-rich chondrule (Fig. 11). This heterogeneity may be related to refractory precursors of Al-rich chondrules, which has also been concluded by Maruyama et al. (1999) who found extreme ^{16}O enrichments for spinel grains in two Allende (CV3) chondrules.

Noble Gas, Carbon, and Nitrogen Abundances and Isotopic Compositions, CRE Age of SG 009

Detailed stepwise combustion results for noble gas, carbon, and nitrogen abundances and isotopic compositions of SG 009 are listed in Table 9.

^{20}Ne, ^{36}Ar, and ^{40}Ar contents are 28.3, 18.2, and 3987.8 ($\times 10^{-7}$ cm^3 STP g^{-1}), respectively. Ne isotope data points form a trend reflecting a mixture of solar wind and the cosmogenic component. The contribution from cosmogenic neon is more pronounced at the late combustion steps (Fig. 12). The low temperature steps of SG 009 having weathering grade W2 show terrestrial Ar contamination typical of desert meteorites (Fig. 13; Korochantseva et al. 2005). $^{40}Ar/^{36}Ar$ ratios of temperature steps ≥700 °C (except for 1100 °C) are constant (53–56) and characterize the argon isotopic composition of this meteorite without atmospheric contamination (Fig. 13).

The C and N abundances of the step-combusted SG 009 are 1628 and 61 ppm, respectively. Bulk $\delta^{13}C$ (+1.6‰; Fig. 14) and $\delta^{15}N$ (+14.4‰; Fig. 15) are in the range observed for EH chondrites and OCs, respectively (Table 10). Note that low temperature steps are possibly contaminated by terrestrial carbon and nitrogen (as in the case of argon) that can influence on average C and N contents and isotopic compositions.

The concentration of cosmogenic ^{21}Ne is 6.93×10^{-8} cm^3 STP g^{-1} comprising 97.0% of $^{21}Ne_{total}$ and calculated using the endmember compositions of SW Ne with $^{20}Ne/^{22}Ne = 13.78$ and $^{21}Ne/^{22}Ne = 0.0329$

Table 6. Siderophile element abundances in metal of SG 009 by LA-ICP-MS.

	101-G	102-G	103-G	104-G	105-G	106-G	107-G	108-G	109-G	110-G	111-G	112-G	113-G
Si (wt%)	0.05	0.04	0.05	0.06	0.06	0.04	*0.02*	0.04	0.06	0.06	0.04	0.04	0.05
P (wt%)	0.037	0.030	0.042	0.042	0.029	0.037	0.031	0.054	0.035	0.019	0.028	0.034	0.017
V (ppm)	b.d.	b.d.	b.d.	b.d.	b.d.	b.d.	b.d.	b.d.	b.d.	b.d.	b.d.	b.d.	b.d.
Cr (ppm)	3	*1*	b.d.	b.d.	b.d.	b.d.	b.d.	b.d.	b.d.	b.d.	b.d.	*0.4*	b.d.
Mn (ppm)	1	1	2	1	1	1	5	1	1	3	2	2	2
Fe (wt%)	93.9	94.2	93.9	94.1	94.3	93.9	93.8	94.1	93.9	94.1	94.0	94.1	94.3
Co (wt%)	0.336	0.336	0.337	0.327	0.342	0.334	0.336	0.341	0.335	0.341	0.339	0.334	0.337
Ni (wt%)	5.67	5.38	5.62	5.44	5.21	5.63	5.53	5.40	5.62	5.46	5.60	5.51	5.28
Cu (ppm)	38	35	38	36	36	37	37	35	38	36	39	35	35
Ga (ppm)	16.8	15.5	16.4	15.9	15.6	15.9	16.1	15.9	16.0	15.6	16.9	16.0	15.4
Ge (ppm)	28.8	26.5	26.2	25.8	26.3	25.8	26.0	26.0	26.5	25.9	24.8	25.0	26.4
As (ppm)	4.26	3.92	4.12	4.05	4.39	4.05	3.81	3.76	4.00	4.07	3.72	4.35	4.43
Mo (ppm)	6.22	4.21	4.23	*3.16*	4.39	4.46	*3.49*	5.01	*2.59*	5.07	4.05	4.52	*3.07*
Ru (ppm)	2.57	2.48	2.74	3.45	4.28	3.10	2.72	7.28	2.37	2.95	2.37	2.48	2.88
Rh (ppm)	0.40	0.39	0.46	0.54	0.69	0.40	0.46	1.27	0.40	0.36	0.40	0.42	0.51
Pd (ppm)	2.54	2.83	2.71	2.55	3.56	2.17	2.40	3.95	2.56	2.67	2.33	2.17	2.32
Sn (ppm)	0.41	0.36	0.34	0.39	0.44	0.37	0.36	0.37	0.39	0.45	0.33	0.30	0.32
Sb (ppm)	*0.16*	*0.16*	*0.19*	*0.11*	*0.08*	*0.13*	*0.17*	*0.09*	*0.16*	*0.08*	*0.11*	*0.08*	*0.14*
W (ppm)	0.89	1.35	1.09	1.17	0.85	0.90	0.78	0.70	0.85	0.60	0.65	0.93	0.97
Re (ppm)	0.09	0.12	0.20	0.20	0.28	0.12	0.14	0.57	0.06	0.12	0.08	0.19	0.20
Os (ppm)	0.92	0.86	2.33	1.75	3.14	1.95	1.08	5.22	0.87	1.08	1.15	1.74	2.29
Ir (ppm)	0.86	1.00	1.91	1.50	2.54	1.46	0.96	4.67	1.00	1.23	1.07	1.75	1.89
Pt (ppm)	2.27	2.32	4.29	3.75	5.78	3.28	2.88	10.66	2.65	2.50	3.00	3.00	3.78
Au (ppm)	0.60	0.69	0.55	0.67	0.64	0.58	0.55	0.62	0.52	0.62	0.73	0.67	0.66

114-G	115-G	116-G	117-G	118-G	119-G	120-G	121-G	122-G	123-G	124-G	125-G	127-G	128-G	Metal average	D.L.
0.03	0.04	0.05	0.04	0.04	*0.02*	0.08	*0.03*	*0.01*	*0.02*	*0.01*	b.d.	b.d.	b.d.	0.04	*0.03*
0.025	0.022	0.017	0.023	0.031	0.038	0.030	0.043	0.033	0.028	0.037	0.032	0.028	0.030	0.032	*0.003*
b.d.	b.d.	b.d.	b.d.	b.d.	b.d.	b.d.	b.d.	b.d.	b.d.	b.d.	b.d.	1	b.d.	1	*0.4*
b.d.	b.d.	b.d.	*0.8*	b.d.	b.d.	b.d.	b.d.	b.d.	b.d.	b.d.	*0.13*	23	4	5	*1*
3	2	2	2	2	2	4	6	2	3	3	3	2	*1*	2	*1*
94.2	94.1	94.1	94.0	94.3	93.9	93.8	93.9	94.2	94.3	94.0	94.1	94.0	94.3	94.1	
0.336	0.342	0.337	0.339	0.333	0.339	0.337	0.337	0.337	0.338	0.328	0.337	0.333	0.320	0.336	
5.39	5.52	5.46	5.61	5.26	5.70	5.69	5.65	5.39	5.33	5.60	5.47	5.62	5.37	5.50	
37	36	35	36	34	38	36	39	37	36	39	39	39	38	37	*2*
17.1	16.2	16.0	16.2	15.4	16.6	16.0	16.5	16.6	16.3	16.2	16.6	16.5	15.5	16.1	*0.2*
25.5	25.3	25.2	23.9	25.6	25.6	24.2	25.1	28.0	25.2	24.5	25.1	25.7	25.0	25.7	*0.2*
3.92	3.94	4.05	3.75	3.98	4.13	4.00	4.19	3.50	4.02	3.66	3.55	3.89	4.00	3.98	*1.20*
4.43	4.35	4.36	*3.63*	5.72	5.16	*3.45*	7.18	5.97	5.71	5.54	*3.21*	*3.13*	*3.04*	4.42	*4*
2.42	2.11	2.54	2.43	2.22	2.67	1.70	3.39	4.13	6.14	2.20	2.21	1.94	2.92	2.99	*0.04*
0.30	0.40	0.41	0.38	0.44	0.42	0.24	0.73	0.68	0.99	0.33	0.27	0.36	0.53	0.49	*0.01*
2.28	2.11	2.22	1.95	2.43	2.59	2.08	2.68	2.16	2.30	2.23	2.86	2.64	2.57	2.51	*0.05*
0.63	0.39	0.47	0.39	0.36	0.42	0.32	0.43	0.42	0.32	0.37	0.41	0.36	0.31	0.39	*0.05*
0.20	*0.07*	*0.12*	*0.12*	*0.15*	*0.11*	*0.12*	*0.12*	*0.12*	*0.12*	*0.06*	*0.08*	*0.08*	*0.14*	*0.12*	*0.2*
0.41	0.56	0.76	0.66	1.09	0.48	0.37	0.60	0.86	0.51	0.74	0.29	0.56	0.85	0.76	*0.01*
0.03	0.09	0.11	0.06	0.08	0.14	0.06	0.23	0.31	0.56	0.14	0.09	0.06	0.19	0.17	*0.01*
0.86	1.26	0.77	0.82	1.59	1.53	0.44	2.12	2.51	4.52	0.75	0.96	0.95	1.72	1.67	*0.001*
0.93	1.42	0.82	0.99	1.17	1.24	0.53	1.86	1.97	4.47	0.70	0.82	0.64	1.65	1.52	*0.003*
2.89	2.81	2.46	1.62	3.00	2.84	1.76	4.59	5.19	9.66	1.83	2.14	2.34	3.51	3.59	*0.01*
0.51	0.53	0.63	0.60	0.58	0.56	0.62	0.60	0.62	0.61	0.59	0.60	0.63	0.60	0.61	*0.03*

D.L. = detection limit; b.d. = below detection.
Values in italics are at the detection limit.

Table 7. Representative elemental compositions of SG 009 chondrule fragments (85-G–109-G, rasters; 129-G–136-G, spots) and sulfides (110-G–114-G, spots) where major elements in weight%, trace elements in ppm; b.d. = below detection, n.d. = not determined

Object name	85-G	89-G	96-G	97-G	98-G	99-G	100-G	101-G	102-G	103-G
SiO_2	53.26	60.60	59.61	54.55	56.21	52.06	55.49	50.68	54.76	56.24
TiO_2	0.134	0.051	0.073	0.087	0.026	0.084	0.026	0.069	0.195	0.093
Al_2O_3	3.71	0.98	1.34	1.20	1.81	1.36	0.19	0.51	1.39	1.09
FeO_T	5.00	3.54	3.37	5.70	5.63	9.08	7.22	10.59	4.85	3.54
MnO	0.188	0.192	0.176	0.203	0.169	0.167	0.112	0.180	0.230	0.197
MgO	32.97	32.60	33.17	35.05	34.33	32.91	35.88	34.62	32.92	35.93
CaO	3.00	1.47	1.30	2.62	0.71	3.49	0.92	1.23	5.04	2.31
Na_2O	0.60	0.23	0.55	0.30	0.84	0.37	0.07	0.11	0.43	0.41
K_2O	0.02	0.03	0.24	0.03	0.08	0.03	0.01	0.01	0.04	0.05
P_2O_5	0.022	0.001	0.003	0.007	0.011	0.028	0.036	0.069	0.004	0.013
S	1.09	0.30	0.17	0.25	0.18	0.42	0.05	1.92	0.15	0.13
Li	7	12	7	11	4	20	8	12	13	7
Be	0.055	0.043	0.060	0.039	0.071	0.047	b.d.	b.d.	0.009	0.015
B	3.61	3.10	2.45	23.43	4.24	30.34	3.27	15.58	11.47	6.41
Sc	10	5	6	8	5	9	3	6	19	12
V	53	43	35	30	10	25	34	60	63	17
Cr	2888	2850	1190	1389	825	1136	2108	2854	2145	889
Co	96	46	60	104	180	146	135	283	75	58
Ni	1969	986	752	1399	2569	2244	2192	3455	1139	868
Cu	35	6	5	6	12	5	1	72	2	9
Zn	23	17	19	20	24	17	13	20	21	28
Ga	0.76	0.22	0.04	0.10	0.06	0.29	0.07	0.27	0.14	0.23
Ge	0.34	0.04	0.02	0.03	0.05	0.12	0.08	0.30	0.03	0.16
As	0.07	0.00	0.04	0.05	0.02	0.03	0.01	0.05	0.01	0.05
Se	1.63	0.35	0.26	0.44	0.32	0.40	0.05	2.69	0.20	0.29
Rb	0.4	0.9	6.2	0.6	1.0	0.5	0.4	0.2	0.6	1.0
Sr	158.7	24.0	39.6	185.2	34.6	149.5	13.7	114.8	143.1	70.3
Y	1.8	1.2	1.3	1.9	0.6	2.3	0.4	1.1	4.1	2.4
Zr	5.0	2.7	3.9	4.3	2.1	5.9	0.9	2.4	6.6	5.3
Nb	0.16	0.19	0.13	0.06	0.02	0.10	0.02	0.07	0.08	0.03
Mo	0.21	0.04	0.10	0.25	0.11	0.28	0.08	0.32	0.11	0.28
Ag	0.03	0.02	0.02	0.08	0.03	0.03	0.02	0.03	0.01	0.03
Cd	0.04	0.01	0.02	0.05	0.04	0.04	0.02	0.02	0.03	0.02
In	0.006	0.001	0.002	0.005	0.002	0.004	0.016	0.001	0.002	0.005
Sn	0.04	0.03	0.03	0.07	0.07	0.07	0.10	0.12	0.08	0.07
Sb	0.02	0.01	0.01	0.01	0.01	0.16	0.01	0.01	0.01	0.01
Cs	0.04	0.07	0.09	0.04	0.05	0.05	0.05	0.04	0.15	0.06
Ba	4.91	1.74	9.74	4.48	7.23	3.56	0.55	1.65	4.14	3.69
La	0.46	0.18	0.16	0.26	0.13	0.42	0.06	0.19	0.29	0.23
Ce	1.27	0.58	0.55	0.91	0.41	1.38	0.28	0.62	1.21	0.87
Pr	0.15	0.08	0.07	0.12	0.05	0.19	0.03	0.08	0.22	0.13
Nd	0.66	0.37	0.36	0.60	0.20	0.87	0.13	0.36	1.26	0.71
Sm	0.18	0.12	0.13	0.19	0.06	0.26	0.04	0.11	0.48	0.26
Eu	0.13	0.04	0.06	0.05	0.08	0.06	0.00	0.01	0.06	0.04
Gd	0.248	0.170	0.173	0.257	0.074	0.341	0.052	0.139	0.668	0.350
Tb	0.042	0.029	0.031	0.045	0.013	0.057	0.012	0.025	0.116	0.061
Dy	0.302	0.201	0.222	0.314	0.091	0.395	0.064	0.185	0.792	0.422
Ho	0.066	0.044	0.050	0.070	0.022	0.085	0.016	0.042	0.165	0.089
Er	0.208	0.135	0.157	0.221	0.066	0.261	0.054	0.139	0.468	0.266
Tm	0.030	0.019	0.023	0.032	0.010	0.037	0.009	0.021	0.062	0.037
Yb	0.233	0.148	0.184	0.224	0.098	0.259	0.073	0.164	0.418	0.246
Lu	0.036	0.023	0.025	0.043	0.012	0.040	0.012	0.028	0.059	0.041

Table 7. *Continued*. Representative elemental compositions of SG 009 chondrule fragments (85-G–109-G, rasters; 129-G–136-G, spots) and sulfides (110-G–114-G, spots) where major elements in weight%, trace elements in ppm; b.d. = below detection, n.d. = not determined.

Object name	85-G	89-G	96-G	97-G	98-G	99-G	100-G	101-G	102-G	103-G
Hf	0.162	0.077	0.111	0.127	0.095	0.169	0.022	0.071	0.273	0.165
Ta	0.017	0.010	0.013	0.012	0.004	0.016	0.003	0.007	0.013	0.016
W	0.010	0.003	0.004	0.009	0.005	0.007	0.013	0.012	0.003	0.020
Tl	0.001	0.000	0.001	0.002	0.001	0.001	0.001	0.002	0.000	0.001
Pb	0.067	0.105	0.058	0.069	0.100	0.138	0.507	0.201	0.215	0.105
Bi	0.009	0.004	0.005	0.003	0.008	0.005	0.034	0.003	0.005	0.021
Th	0.045	0.023	0.032	0.039	0.025	0.053	0.008	0.024	0.028	0.032
U	0.017	0.010	0.014	0.026	0.006	0.017	0.014	0.008	0.023	0.010

104-G	105-G	106-G	107-G	108-G	109-G	129-G	130-G	131-G	132-G	133-G
56.03	57.81	54.24	57.94	58.43	55.52	48.87	48.08	47.10	45.02	57.40
0.042	0.013	0.125	0.114	0.122	0.133	0.231	0.208	0.257	0.146	0.119
0.38	0.18	2.21	1.71	1.98	1.44	3.05	4.33	5.15	3.83	2.49
3.09	7.83	7.40	1.71	1.69	4.27	3.58	1.59	4.01	1.60	2.02
0.165	0.189	0.629	0.197	0.213	0.212	0.194	0.169	0.152	0.163	0.244
37.64	31.15	29.56	33.87	34.18	33.35	40.20	41.74	38.17	45.85	34.42
2.42	2.48	4.44	2.68	2.10	3.48	3.56	3.14	4.46	2.71	2.34
0.13	0.14	0.94	0.68	0.88	0.47	0.29	0.70	0.66	0.66	0.89
0.01	0.03	0.09	0.40	0.14	0.27	0.01	0.03	0.03	0.03	0.06
0.005	0.005	0.006	0.002	0.002	0.008	0.008	0.009	0.010	0.009	0.000
0.08	0.16	0.35	0.70	0.26	0.84	n.d.	n.d.	n.d.	n.d.	n.d.
8	23	12	6	5	7	9	4	7	6	5
0.016	0.007	0.008	0.012	0.017	0.029	0.059	0.045	0.070	0.044	0.042
16.86	0.98	50.57	23.15	33.36	212.67	152	19	123	32	35
6	2	10	10	10	13	22	19	21	14	12
10	56	89	19	63	30	97	84	85	66	66
631	4078	5809	1348	2831	1557	2742	2294	2676	1775	3632
28	65	48	14	29	139	84	24	85	21	22
389	1064	1267	205	429	1949	1245	221	1407	371	342
1	4	5	9	7	14	5	9	11	5	20
17	10	9	57	17	88	25	25	21	24	20
0.07	0.34	0.33	0.04	0.13	0.16	0.17	0.08	0.12	0.07	0.13
0.02	0.08	0.03	0.03	0.03	0.07	0.02	0.01	0.02	-0.01	0.06
0.00	0.04	0.01	0.00	3.73	71.70	0.40	0.10	0.53	0.21	2.52
0.16	0.21	0.40	1.09	0.31	0.89	n.d.	n.d.	n.d.	n.d.	n.d.
0.3	0.9	1.5	8.8	2.9	7.0	0.4	0.9	0.6	0.8	2.1
127.2	49.2	70.5	79.3	69.8	138.1	118.1	29.9	76.4	38.3	88.9
1.0	0.5	2.4	1.7	2.1	3.1	5.1	4.6	6.5	3.5	3.1
2.7	1.1	5.7	6.0	5.2	7.9	8.1	12.1	14.9	11.4	7.6
0.02	0.04	0.48	0.06	0.46	0.10	0.36	0.76	0.90	0.74	0.42
0.16	0.06	0.50	0.15	1.72	6.18	1.19	0.10	1.46	0.25	2.14
0.01	0.04	0.05	0.03	0.07	0.08	0.03	0.03	0.03	0.02	0.06
0.02	0.02	0.02	0.02	0.08	0.26	0.03	0.01	0.01	0.01	0.05
0.005	0.009	0.001	0.002	0.001	0.010	0.001	b.d.	b.d.	b.d.	b.d.
0.04	0.05	0.03	0.02	0.02	0.07	0.02	0.02	0.02	0.02	0.02
0.01	0.01	0.01	0.01	0.03	0.35	0.02	0.01	0.03	0.01	0.03
0.03	0.06	0.07	0.11	0.13	0.08	0.03	0.02	0.04	0.02	0.22
2.44	1.37	7.59	16.78	11.14	43.87	5.64	3.80	9.68	5.27	8.99
0.17	0.09	0.38	0.16	0.33	0.38	0.469	0.732	0.824	0.682	0.448
0.55	0.46	1.19	0.61	1.10	1.27	1.434	1.970	2.279	1.777	1.354
0.08	0.06	0.17	0.09	0.15	0.19	0.235	0.279	0.360	0.243	0.181
0.36	0.28	0.82	0.49	0.70	1.00	1.260	1.409	1.807	1.164	0.902

Table 7. *Continued*. Representative elemental compositions of SG 009 chondrule fragments (85-G–109-G, rasters; 129-G–136-G, spots) and sulfides (110-G–114-G, spots) where major elements in weight%, trace elements in ppm; b.d. = below detection, n.d. = not determined.

104-G	105-G	106-G	107-G	108-G	109-G	129-G	130-G	131-G	132-G	133-G
0.10	0.08	0.23	0.18	0.19	0.32	0.453	0.400	0.582	0.337	0.231
0.01	0.01	0.08	0.07	0.08	0.07	0.053	0.129	0.122	0.136	0.115
0.145	0.084	0.353	0.247	0.318	0.491	0.660	0.629	0.942	0.524	0.444
0.024	0.015	0.063	0.043	0.055	0.084	0.114	0.109	0.168	0.094	0.080
0.169	0.093	0.430	0.300	0.371	0.559	0.802	0.772	1.140	0.642	0.540
0.038	0.019	0.091	0.065	0.079	0.120	0.181	0.163	0.246	0.132	0.113
0.115	0.056	0.280	0.191	0.250	0.351	0.565	0.520	0.763	0.443	0.376
0.017	0.008	0.040	0.027	0.035	0.046	0.080	0.070	0.099	0.060	0.051
0.126	0.072	0.247	0.171	0.181	0.263	0.552	0.469	0.677	0.400	0.293
0.021	0.008	0.044	0.029	0.038	0.048	0.090	0.078	0.108	0.066	0.055
0.080	0.027	0.163	0.177	0.147	0.231	0.258	0.336	0.432	0.326	0.236
0.010	0.004	0.021	0.019	0.020	0.025	0.024	0.037	0.045	0.042	0.024
0.003	0.016	0.001	0.002	0.014	0.179	0.056	0.120	0.186	0.155	0.013
0.000	0.001	0.001	0.001	0.005	0.056	0.001	0.001	0.002	0.002	0.004
0.049	0.625	0.385	0.068	0.086	0.234	0.184	0.323	0.355	0.362	0.108
0.002	0.013	0.007	0.002	0.012	0.007	0.003	0.003	0.007	0.005	0.001
0.021	0.007	0.047	0.043	0.043	0.055	0.051	0.089	0.112	0.103	0.066
0.008	0.017	0.025	0.015	0.120	1.040	0.120	0.016	0.103	0.029	0.078

134-G	135-G	136-G		110-G	111-G	112-G	113-G	114-G	Detection limit
56.12	57.84	55.54	Si	0.15	0.51	0.21	0.61	1.09	*0.005*
0.050	0.105	0.063	Ti	0.003	0.004	0.003	0.003	0.003	*0.0001*
0.53	2.10	0.64	Al	0.01	0.08	0.01	0.01	0.02	*0.001*
2.98	1.42	3.91	Fe	51.72	44.43	44.89	44.57	42.08	*0.0001*
0.183	0.203	0.392	Mn	0.410	0.397	0.351	0.236	0.400	*0.00001*
38.80	33.00	36.64	Mg	0.17	0.35	0.28	0.18	0.92	*0.0005*
1.20	3.81	2.56	Ca	0.76	0.29	0.20	0.05	0.48	*0.002*
0.11	1.01	0.22	Na	0.57	0.13	0.15	0.20	0.24	*0.002*
0.03	0.51	0.03	K	0.14	0.03	0.04	0.05	0.06	*0.002*
0.003	0.001	0.004	P	0.096	0.028	0.001	0.028	0.001	*0.0001*
n.d.	n.d.	n.d.	S	30.10	39.81	40.33	40.26	40.39	*0.001*
6	7	8	Li	141	13	18	17	28	*0.07*
0.032	0.025	0.032	Be	b.d.	b.d.	b.d.	b.d.	b.d.	*0.02*
58	30	67	B	28.18	1.61	1.09	0.95	20.05	*0.03*
6	12	9	Sc	2.4	2.0	1.2	0.7	0.4	*0.2*
46	19	75	V	855	765	639	499	1059	*0.001*
1871	1351	3067	Cr	68648	35680	34685	30028	60851	*0.04*
40	10	28	Co	272	26	51	118	83	*0.01*
688	252	412	Ni	10,406	1093	1123	6788	2652	*0.06*
4	12	5	Cu	510	732	375	366	1582	*0.2*
15	99	22	Zn	65	59	63	11	84	*0.02*
0.11	0.05	0.43	Ga	2.78	0.70	0.28	0.14	1.08	*0.01*
0.02	0.00	0.00	Ge	1.27	1.30	1.15	1.05	1.09	*0.02*
1.89	0.01	0.04	As	0.26	0.10	0.09	0.24	0.08	*0.003*
n.d.	n.d.	n.d.	Se	71.05	58.51	59.22	55.52	58.48	*0.1*
1.7	11.5	0.5	Rb	1.1	0.5	0.5	1.0	0.7	*0.02*
26.7	108.8	92.0	Sr	113.5	30.0	27.9	3.3	104.4	*0.004*
0.7	2.2	1.3	Y	0.0	0.1	0.0	0.0	0.0	*0.003*
1.7	7.6	2.1	Zr	0.1	0.2	0.1	0.1	0.1	*0.004*
0.03	0.05	0.04	Nb	0.60	0.54	0.54	0.66	0.58	*0.0005*

Table 7. *Continued*. Representative elemental compositions of SG 009 chondrule fragments (85-G–109-G, rasters; 129-G–136-G, spots) and sulfides (110-G–114-G, spots) where major elements in weight%, trace elements in ppm; b.d. = below detection, n.d. = not determined.

134-G	135-G	136-G		110-G	111-G	112-G	113-G	114-G	Detection limit
0.96	0.14	0.30	Mo	4.57	1.32	1.50	3.93	5.56	*0.01*
0.03	0.04	0.03	Ag	0.24	0.30	0.21	0.60	0.44	*0.001*
0.10	0.01	b.d.	Cd	0.07	0.09	0.06	0.17	0.04	*0.002*
b.d.	b.d.	b.d.	In	b.d.	b.d.	b.d.	0.4981	b.d.	*0.0009*
0.03	0.02	0.02	Sn	0.02	0.02	0.01	1.38	0.01	*0.004*
0.03	0.00	0.01	Sb	0.02	0.01	0.02	1.13	0.01	*0.001*
0.07	0.17	0.03	Cs	0.11	0.10	0.10	0.25	0.12	*0.02*
2.70	20.39	3.13	Ba	0.36	0.47	0.21	0.87	0.60	*0.001*
0.095	0.203	0.141	La	0.003	0.012	0.003	0.037	0.009	*0.002*
0.287	0.673	0.479	Ce	0.003	0.028	0.009	0.228	0.032	*0.0003*
0.038	0.104	0.068	Pr	0.001	0.006	0.002	0.072	0.004	*0.0003*
0.192	0.571	0.350	Nd	0.003	0.044	0.017	0.082	0.022	*0.001*
0.061	0.244	0.121	Sm	0.002	0.015	0.003	0.109	0.005	*0.001*
0.013	0.096	0.017	Eu	0.004	0.009	0.001	0.008	0.002	*0.001*
0.096	0.334	0.165	Gd	0.002	0.024	0.002	0.002	0.005	*0.003*
0.019	0.061	0.029	Tb	0.000	0.004	0.001	0.037	0.002	*0.0008*
0.128	0.395	0.214	Dy	0.003	0.024	0.005	0.016	0.009	*0.001*
0.032	0.089	0.055	Ho	0.000	0.004	0.001	0.003	0.001	*0.0002*
0.087	0.277	0.176	Er	0.001	0.007	0.003	0.006	0.007	*0.0009*
0.016	0.039	0.027	Tm	0.002	0.003	0.002	0.006	0.003	*0.0008*
0.111	0.211	0.217	Yb	0.002	0.011	0.002	0.012	0.006	*0.0009*
0.023	0.037	0.035	Lu	0.000	0.001	0.000	0.003	0.001	*0.0005*
0.060	0.253	0.066	Hf	0.001	0.007	0.005	0.012	0.006	*0.002*
0.003	0.023	0.008	Ta	0.001	0.001	0.001	0.062	0.000	*0.0007*
0.008	0.001	0.003	W	0.011	0.004	0.002	0.083	0.009	*0.003*
0.002	0.001	0.000	Tl	0.004	0.002	0.001	0.111	0.001	*0.0007*
0.042	0.077	0.877	Pb	0.201	0.114	0.202	0.561	0.186	*0.0007*
0.002	0.001	0.019	Bi	0.008	0.004	0.007	0.525	0.004	*0.0006*
0.020	0.056	0.025	Th	0.001	0.001	0.001	0.001	0.001	*0.0003*
0.031	0.014	0.010	U	0.002	0.001	0.001	0.412	0.002	*0.0002*

(Heber et al. 2009) and cosmogenic Ne with $^{20}Ne/^{22}Ne = 0.8$ (Eugster and Michel 1995) and $^{21}Ne/^{22}Ne = 0.90$ (see the caption of Fig. 12). The minimum CRE age of 24 Ma was calculated for SG 009 from the maximum P_{21} of 0.29×10^{-8} cc gMa^{-1} for the meteoroid with radius of 40–50 cm by the model of Leya and Masarik (2009) and the bulk composition of chondrite calculated from mineral composition and modes. For comparison, metal-rich carbonaceous chondrites Isheyevo (CH/CB_b) and Bencubbin (CB_a) have CRE ages of 34 Ma and 39 ± 3Ma, respectively, some CH chondrites have rather young CREs (HaH 237 [CB_b] 3 Ma; PAT 91546 [CH] >8 Ma; PCA 92468 [CH] 4.3 Ma; RKP 02435 [CH] 1.5 Ma; Weber et al. 2001). The CRE age of SG 009 is usual for O, E, and R chondrites having the range up to 50–80 Ma and close to carbonaceous chondrites (Wieler 2002).

DISCUSSION

A New Grouplet of GCs

SG 009 is a new metal-rich chondrite breccia which has characteristics similar to those of other metal-rich chondrites NWA 5492 and GRO 95551. Weisberg et al. (2015) distinguished these as a new grouplet of GCs named from the first found meteorite of this grouplet, GRO 95551. SG 009 is here identified as the third member of the GCs. Matrix is absent in all three GCs similar to other metal-rich chondrites including CH-CB and NWA 12379/12273 meteorites. Like other GCs, SG 009 does not contain matrix lumps that occur in CH-CB chondrites and there is no matrix material interstitial to the chondrules and metal. GCs contain PO, PP, POP, BO, RP, Al-rich, and SiO_2-rich

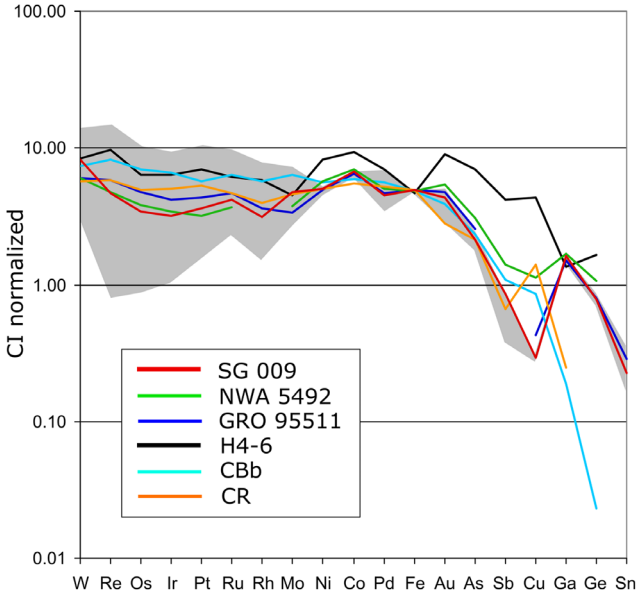

Fig. 8. Siderophile element distribution in metal of SG 009, NWA 5492, and GRO 95551 (Campbell and Humayun 2003; Weisberg et al. 2015), H4-6 (Kong and Ebihara 1997), CBb (Campbell et al. 2001), E chondrite (Kong et al. 1997), and CR chondrites (Kong et al. 1999) relative to CI composition (Anders and Grevesse 1989). The shadow gray area is a range of the SG 009 metal composition (Color figure can be viewed at wileyonlinelibrary.com.)

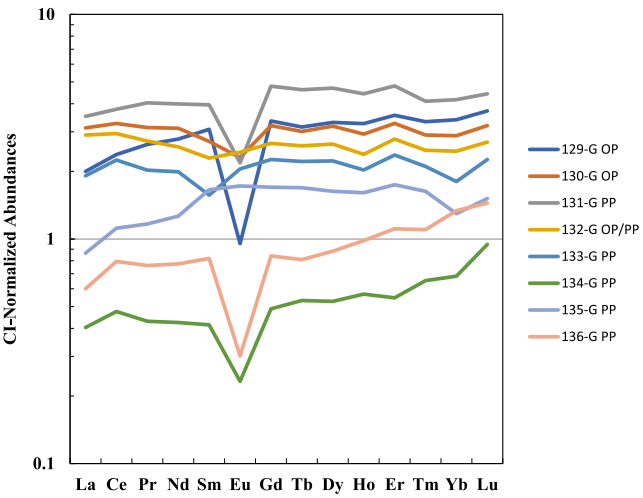

Fig. 9. Representative CI-normalized (Anders and Grevesse 1989) abundances of REEs of silicate chondrules from SG 009. OP—olivine porphyritic, PP—pyroxene porphyritic, PP/OP—olivine pyroxene porphyritic chondrules (129-G–136-G—numbers of chondrules). (Color figure can be viewed at wile yonlinelibrary.com.)

chondrules, with PP chondrules being strongly predominant. No refractory inclusions have been observed in any G chondrites.

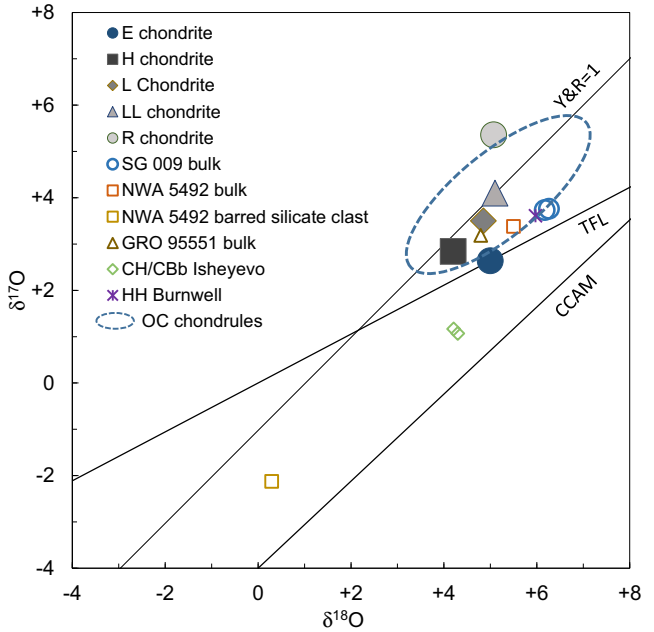

Fig. 10. Bulk oxygen isotopic compositions (‰) of SG 009 compared to bulk values of two other G chondrites NWA 5492 and GRO 95551 (Weisberg et al. 2012, 2015), HH chondrite Burnwell (Russell et al. 1998), CH/CBb Isheyevo (Ivanova et al. 2008), as well as average values of ordinary (Clayton et al. 1991), enstatite (Clayton et al. 1984) chondrites, and Rumuruti (Bischoff et al. 1994). (Color figure can be viewed at wileyonlinelibrary.com.)

SG 009 and the two other G-type meteorites are characterized by a high content of metal (>20 vol%) like CH chondrites, more than in ordinary (OC) and enstatite (EC) chondrites (5–15 vol%), HH, and low-FeO ordinary chondrites (Russell et al. 1998; Troiano et al. 2011), but less than in CB chondrites (up to 70 vol%) and ungrouped metal-rich chondrites NWA 12379/12273 (~64 vol%; Agee et al. 2019; Jansen et al. 2019). Fe,Ni-metal in SG 009 is similar to that of NWA 5492 in Ni and Co contents, but differs from that of GRO 95551 having both high-Ni and low-Ni metal (Weisberg et al. 2015). None of the G chondrites have solar Co/Ni ratios unlike CH-CB chondrites (Fig. 7), and the Si, Cr, and P contents of the metal are low (below our electron probe detection limit of 0.03 wt%), unlike metal in enstatite chondrites (e.g., Keil 1968; Table 4). G chondrites do not contain any zoned Fe,Ni-metal like that in the CH and CBb chondrites.

Among the G chondrites, only SG 009 contains PGE metal inclusions that were not described in NWA 5492 or in GRO 95551. The PGE nuggets may be products of transformation of primary refractory material similar to metal nuggets in CVs or products of metal oxidization (e.g., Blum et al. 1989). The fact that PGE metal particles are surrounded by calcite may

Table 8. Oxygen isotopic compositions of SG 009 Ol, Px, and an Al-rich chondrule (Ol, Sp)

	ID	Phase	$\delta^{17}O$	1σ	$\delta^{18}O$	1σ	$\Delta^{17}O$	1σ
Ol, Px	G18C	ol	+4.47	0.25	+5.38	0.06	+1.62	0.26
	G18D	ol	+3.70	0.28	+4.86	0.07	+1.13	0.28
	G18E	ol	+3.07	0.20	+4.55	0.07	+0.67	0.20
	G9A	ol	+2.84	0.31	+4.48	0.09	+0.47	0.31
	OL	ol	+2.59	0.29	+3.45	0.07	+0.78	0.30
	G9C	ol	+3.29	0.32	+5.25	0.07	+0.52	0.32
	G9D	ol	+3.47	0.20	+5.56	0.08	+0.53	0.21
	G18A	px	+3.94	0.25	+6.33	0.09	+0.59	0.25
	G18B	px	+3.55	0.31	+5.79	0.06	+0.50	0.31
	G18F	px	+4.53	0.26	+7.40	0.09	+0.63	0.27
	G18G	px	+4.73	0.21	+7.30	0.08	+0.87	0.21
	G18H	px	+4.15	0.35	+7.32	0.07	+0.29	0.35
	G18I	px	+3.99	0.30	+7.05	0.07	+0.27	0.30
Al-rich chondrule	G1B	ol	−1.47	0.35	+0.14	0.05	−1.54	0.35
	G1H	ol	−0.19	0.29	+2.02	0.07	−1.26	0.30
	G1I	ol	+1.47	0.40	+3.25	0.15	−0.25	0.40
	G1A	sp	−1.74	0.33	−1.04	0.08	−1.19	0.33
	G1C	sp	−1.77	0.29	−0.94	0.07	−1.27	0.29
	G1D	sp	−1.30	0.29	−1.63	0.06	−0.44	0.30
	G1E	sp	−1.07	0.28	−1.29	0.08	−0.39	0.29
	G1G	sp	−0.69	0.31	−0.98	0.10	−0.18	0.31

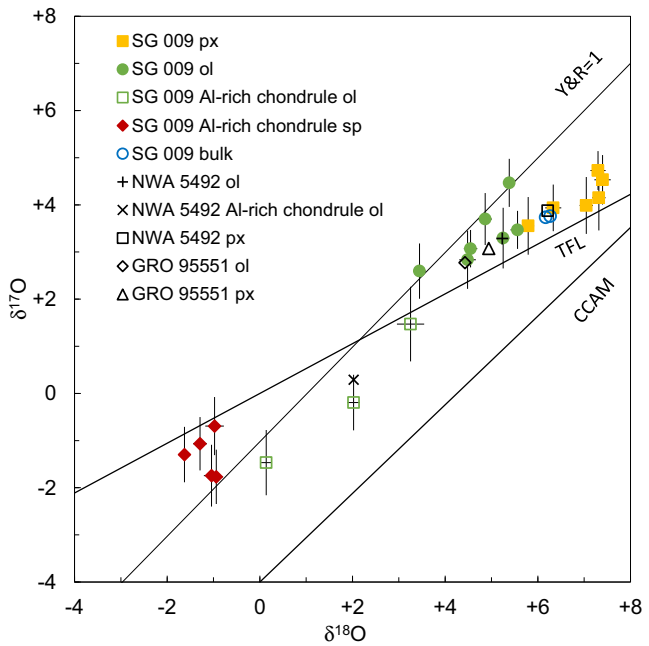

Fig. 11. Oxygen isotopic compositions (‰) of olivine and pyroxene from several POP chondrules, and of olivine and spinel from an Al-rich chondrule from SG 009 compared to bulk oxygen isotopic composition of SG 009, and mean values of NWA 5492 and GRO 95551 olivine and pyroxene ion probe data (Weisberg et al. 2012, 2015). ^{16}O-rich composition is best preserved in spinel and likely related to refractory precursor material. (Color figure can be viewed at wileyonline library.com.)

indicate that this oxidization took place in the desert rather than being intrinsic to the meteorite.

Sulfides are more abundant in GCs than in CHs and CBs, but all GCs have a sulfide assemblage (daubréelite, rare alabandite, and Cr-troilite) distinct from that of ECs, oldhamite, alabandite, niningerite, or any of the other unusual sulfides typical of E chondrites (e.g., Keil 1968). The FeO/MnO ratio in enstatite of G chondrites (2.83) compared with the FeO/MnO ratio in enstatite of E chondrites in which MnO, Cr_2O_3, and TiO_2 contents are below a microprobe detection limit (Van Niekirk et al. 2014) that may indicate incomplete reduction of Mn, Cr, and Ti in G chondrites in comparison with E chondrites.

The silicate compositions of SG 009 are very reduced and similar to those of other GCs (Weisberg et al. 2015) and EHs, and they are more reduced than those of CH-CB chondrites (Fa2-4), any other types of ordinary chondrites, HH chondrites (Russell et al. 1998; Troiano et al. 2011), and the metal-rich ungrouped NWA 12379/12273 which have olivine composition like that in L/LL chondrites (Jansen et al. 2019).

All GCs have plagioclase with variable compositions (Table 3) compared to ordinary and enstatite chondrites and NWA 12379/12273 very sodic plagioclase, and compared to CH-CB plagioclase of anorthitic composition. This may indicate selective evaporation of sodium from the melt during impact events. Glasses in chondrule mesostasis of all G

Table 9. Stepwise combustion data for Sierra Gorda 009 (13.44 mg).

T (°C)	$^{20}Ne^{a}$	$^{20}Ne/^{22}Ne$	$^{21}Ne/^{22}Ne$	$^{40}Ar^{a}$	$^{40}Ar/^{36}Ar$	N^{b}	$\delta^{15}N$	C^{b}	$\delta^{13}C$
200	165.2	11.4 (1)	0.0300 (5)	24,107.1	286.0 (3)	14.65	7.41 (23)	31.19	−7.76 (24)
300	19.4	13.7 (1)	–	4233.6	286.7 (1.2)	13.36	10.3 (2)	204.84	−3.63 (13)
400	8.5	12.8 (2)	0.0507 (54)	1287.2	282.5 (3.4)	9.03	18.5 (3)	72.87	−7.43 (25)
500	5.8	11.4 (2)	0.0877 (62)	974.7	279.8 (4.9)	5.15	28.3 (3)	150.67	3.06 (16)
600	5.1	10.4 (2)	0.147 (8)	773.8	265.9 (7.7)	3.62	27.2 (4)	429.39	2.94 (27)
700	4.8	5.79 (8)	0.521 (10)	602.7	53.3 (1)	2.29	31.5 (2)	700.89	3.51 (13)
800	5.1	4.26 (5)	0.632 (10)	488.8	55.4 (1)	1.53	30.3 (3)	10.07	4.42 (1.30)
900	5.4	4.26 (5)	0.633 (9)	475.4	56.6 (1)	1.93	28.8 (3)	9.63	−13.1 (1.1)
1000	5.6	4.94 (6)	0.545 (9)	504.5	56.7 (1)	1.93	23.4 (3)	8.06	n.a.
1100	6.9	5.04 (5)	0.551 (6)	922.6	283.1 (5.8)	1.41	18.2 (3)	2.28	−4.01 (2.40)
1200	8.0	5.13 (5)	0.558 (8)	427.1	57.5 (1)	0.52	10.4 (3)	2.93	−1.38 (54)
1300	10.0	5.38 (5)	0.573 (7)	407.7	56.9 (1)	1.28	−13.7 (3)	3.45	5.95 (47)
1400	33.0	8.56 (5)	0.324 (3)	4672.6	277.3 (1.2)	4.33	−2.52 (35)	1.26	−4.6 (7)
Total	282.8	9.23 (6)	0.4898 (69)	39,878.0	219.0 (7)	61.05	14.4 (3)	1627.52	1.6 (2)

5–10% uncertainty in absolute concentrations of noble gases.
Numbers in parentheses refer to the last digits and are 1σ-uncertainties.
n.a.—not analyzed
[a]$\times 10^{-8}$ cm^3 STP g^{-1}
[b]ppm.

chondrites are enriched in K_2O, TiO_2, CaO, and Na_2O, and the metal-enriched mesostasis was also observed in NWA 5492. Troilite-bearing mesostasis instead of glassy mesostasis was mentioned to be present in NWA 5492 (Weisberg et al. 2012). The metal- and sulfide-rich mesostases in some chondrules indicate that these chondrules may form by melting of sulfide- and metal-rich precursors. These precursors may in turn be formed in a sulfur-bearing vapor.

Among chromite-spinel minerals, Mg-chromite was described only in SG 009; in other G chondrites, NWA 5492 and GRO 95551, chromite was not observed, and all chromium-rich minerals were sulfides—daubreelite and Cr-rich troilite, which are typical minerals of E chondrites. In all GCs, the spinel in Al-rich chondrules occurs together with anorthite, olivine, and Ca-pyroxene.

The G chondrites have variable degrees of shock stages, from S2 (SG 009, NWA 5492) to S3 (NWA 5492 and GRO 95551) based on olivine extinction and the presence or absence of planar fractures (Stoffler et al. 1991). In NWA 5492 section, pyroxene coexisting with olivine is darkened due to inclusions of metal and sulfides (Weisberg et al. 2015). Such silicate darkening may be interpreted as evidence of a moderate degree of shock, and post-shock annealing could have healed the shock features of olivine (e.g., Rubin 2004). Alternatively, the darkening in the pyroxene may be a result of reduction instead of shock effects.

Bulk oxygen isotopic compositions of all G chondrites show a range of $\Delta^{17}O>0$ and are plotted between values for ordinary chondrites and enstatite chondrites in the three-oxygen isotope diagram. The oxygen isotopic compositions of most chondrules and silicate clasts in the G chondrites overlap with chondrules from EH3, LL3, and R3 chondrules (Figs. 10 and 11).

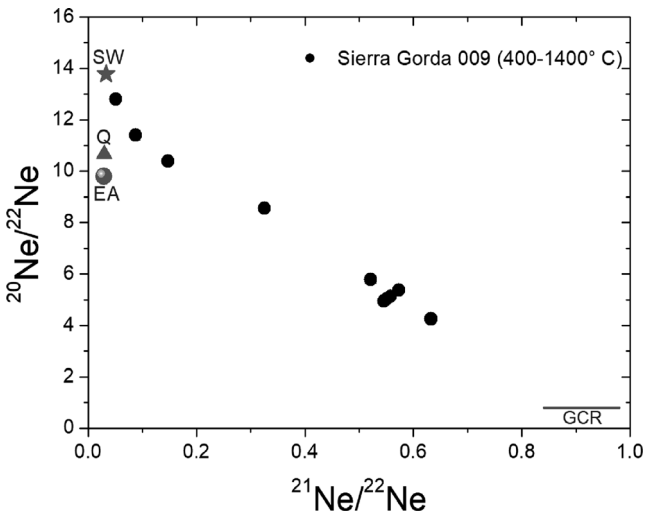

Fig. 12. Three-isotope plot of $^{21}Ne/^{22}Ne$ versus $^{20}Ne/^{22}Ne$ for Sierra Gorda 009. Ne isotope data points form a trend reflecting a mixture of solar wind and the cosmogenic component. The contributions from cosmogenic neon are more pronounced at the late combustion steps. Other components plotted include solar wind (SW; Heber et al. 2009), Earth's atmosphere (EA; Eberhardt et al. 1965), and Q (Ott 2002). The cosmogenic component produced by galactic cosmic rays (GCR) is given: $(^{20}Ne/^{22}Ne)_c$ from Eugster and Michel (1995), $(^{21}Ne/^{22}Ne)_c$ using Leya and Masarik (2009) for the bulk chemical composition of SG 009 calculated from mineral compositions and modes.

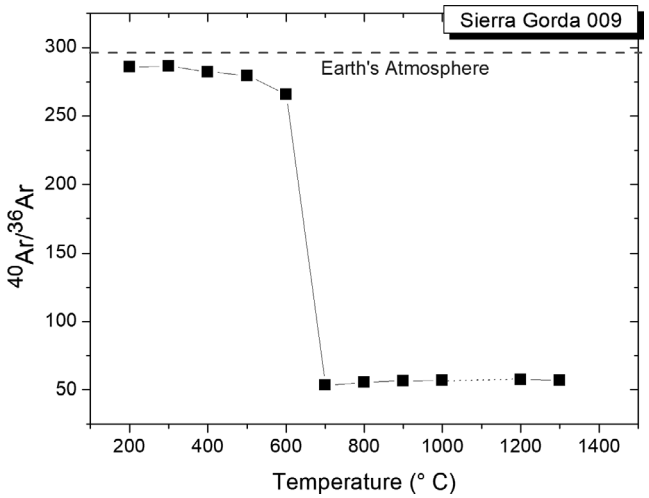

Fig. 13. The $^{40}Ar/^{36}Ar$ ratio variations in temperature steps for Sierra Gorda 009. The value of the temperature step 1100°C is omitted. $^{40}Ar/^{36}Ar$ ratios of temperature steps ≥700°C characterize argon isotopic composition of this meteorite without atmospheric contamination observed at low temperatures.

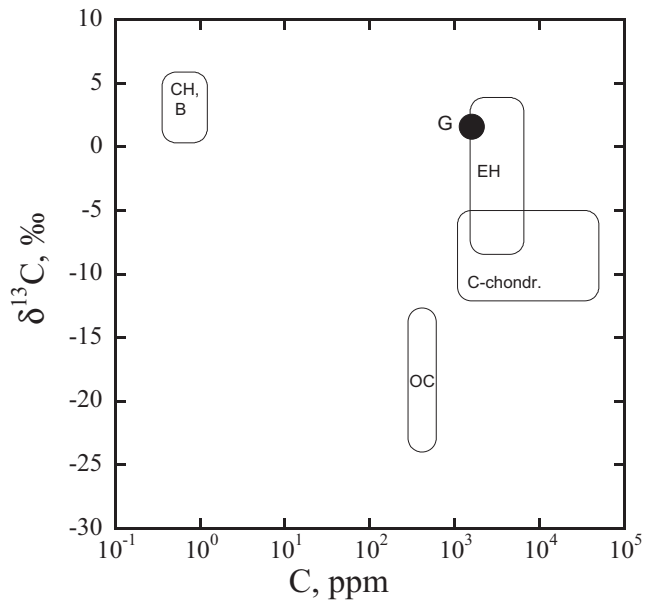

Fig. 14. Carbon abundance and carbon isotopic composition of SG 009 (G) compared to EH, OC, CH/CB, and carbonaceous chondrites (Grady and Wright 2003).

Oxygen isotopic compositions of olivine and pyroxene from SG 009 also plot between EHs and OCs. However, we observed heterogeneity in oxygen isotopic compositions among spinel and olivine of the Al-rich chondrule and of the olivine–pyroxene chondrules, similar to barred silicate clasts (Weisberg et al. 2012) and Allende spinel-rich chondrules (Maruyama et al. 1999).

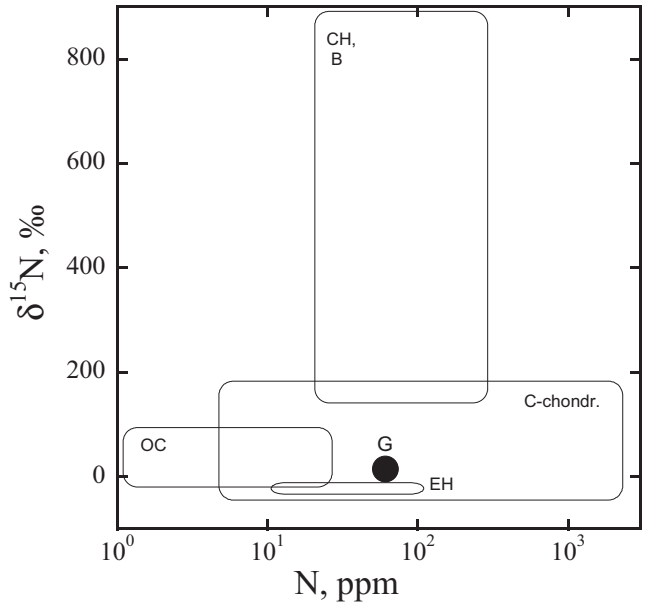

Fig. 15. Nitrogen abundance and nitrogen isotopic composition of SG 009 (G) compared to EH, OC, CH/CB, and carbonaceous chondrites (Grady and Wright 2003).

Table 10. Carbon and nitrogen abundances and isotopic compositions of SG 009. Literature data on other chondrites (Grady and Wright 2003) are given for comparison.

	C (ppm)	$\delta^{13}C$ (‰)	N (ppm)	$\delta^{15}N$ (‰)
Sierra Gorda 009	1628	1.6	61	14.4
OC	300–6000	−24 to −12	1–25	−20 to +100
EH (graphite)	1500–7000	−9 to +4	10–100	−30 to −10
CI, CM, CR	0.4–5 wt%	−12 to −5	500–2000	+20 to +180
CO, CV, CK	0.1–1.1 wt%	−25 to −8	5–200	−50 to +100
CH, Bencubbin	0.35–1.21	+0.3 to +6	20–280	+150 to +900

The spread of the SG 009 data above and below the mass-dependent fractionation line (Fig. 11) can be explained by mixing of material from different oxygen reservoirs and by exchange of oxygen isotopes during melting and crystallization. The precursor of the Al-rich chondrule was probably a CAI with oxygen isotopic composition typical for refractory inclusions (^{16}O–enriched). During melting, evaporation, and isotopic exchange with oxygen between different reservoirs, the primary oxygen isotope compositions were shifted, and as a result of it, formed the observed range of $\Delta^{17}O$ values.

The affinity of SG 009 to E and O chondrites is supported by bulk carbon and nitrogen isotopic data—they have affinity to E and OC chondrites (Grady and Wright 2003). Neon isotopic data reflect a mixture of

cosmogenic and solar components but do not prove helpful in discriminating the variable provenances of components in SG 009. Domination of solar but not planetary noble gases indicates that the analyzed sample has been exposed to solar wind on the surface of the parent body. The CRE age of SG 009 is typical for O, E, and R chondrites.

Metal and Silicate Geochemistry of G Chondrites

The average metal composition of SG 009 in general is in a good agreement with that of the metal in NWA 5492 (Weisberg et al. 2015) and GRO 95551 (Campbell and Humayun 2003) although the GRO 95551 metal is represented by both high-Ni and low-Ni metal (Weisberg et al. 2001). However, there are important differences between the SG 009 metal and NWA 5492 and GRO 95551 metal—SG 009 metal shows a wide range of compatible element abundance (Re, Os, Ir, Pt, Ru; Fig. 8). This may imply that the metal underwent some fractionation, and that we are dealing with differently modified metal particles at surface conditions or in outer space due to several possibilities: sulfidization, partial melting of the metal, and/or formation of small pools of shock melt which crystallized relatively quickly that resulted in a wide spread in siderophile element compositions.

Unlike metal from carbonaceous chondrites, CR, and CH-CB, SG 009 and other G chondrites, NWA 5492 and GRO 95551 have a fractionated refractory siderophile element pattern similar to those in H chondrite (Kong and Ebihara 1997; Teplyakova et al. 2012) that lacks the oxidation losses of Fe, Ni, and Co observed in H4-6 chondrite metal due to more intense reduction in SG 009 metal. The G chondrite metal has siderophile element abundances that are similar to H chondrite bulk composition with the exception of Mo, Ni, Pd, Au, and As whose concentrations are higher than for other siderophiles (Fig. 8). The G chondrite metal does not show the enrichments of Au and As observed in EH and EL metal (Kong et al. 1997) but has a chondritic Au/Ni ratio unlike CR, CH, and CB metal (which have subchondritic Au/Ni ratios). As is seen on a plot of As versus Au (Fig. 16), the SG 009 metal has chondritic composition unlike IIIAB, IVA, and IIAB irons. Ir and Os correlation in metal of SG 009 compared with IVB, and metal of NWA 5492, G-chondrite also indicates chondritic composition (Fig. 17).

Therefore, metal from G chondrites could derive from the H chondrite bulk composition under a higher degree of reduction than the ordinary chondrite metal experienced. A plot of W/Ni (CI) versus Fe/Ni (CI; Fig. 18) shows this degree of reduction of G chondrite metal. On this plot, bulk H chondrite metal plots at a high W/Ni (CI) ratio with a chondritic Fe/Ni (CI) ratio. Metal from unequilibrated and equilibrated LL, L, H (Kong and Ebihara 1997), EL, and EH (Kong et al. 1997) metal plot along a W-Fe trend toward the bulk H chondrite composition trend. Metal compositions from SG 009 display variable W/Ni (CI) composition at constant Fe/Ni(CI) composition, exhibiting both higher and lower W/Ni(CI) ratio relative to the chondritic ratio, while NWA 5492 metal clusters (Weisberg et al. 2015) around the chondritic value (Fig. 18). Thermal re-equilibration may have caused the (W/Ni; CI) ratio to increase (Humayun and Campbell 2002) because W is less siderophile than Fe at $T < 1200$ K and a low metal-silicate ratio during re-equilibration would result in a final W/Ni (CI) >1.

Rare earth element patterns (REEs) in chondrules of SG 009 reflect variable oxygen fugacity environments during chondrule formation. The positive Ce anomaly is an indicator of condensation from a vapor formed by evaporating silicates under oxidizing conditions. Such oxidizing conditions are attained during evaporation of silicates, for example, in vacuum (Wang et al. 2001), although low-pressure nebular environments with high dust-to-gas ratios probably suffice.

The negative Eu and Yb may record volatilization in a gas in reducing conditions more typical of nebular environments. Evidence for a highly reducing environment experienced by SG 009 chondrules is provided by the subchondritic Nb/Ta ratios (9.2 on average, compare to 17.3 in CI) in the silicates where Nb has acted like a chalcophile element, with high concentrations in SG 009 sulfides. Using the equilibrium $Fe + FeSiO_3 + 0.5\ O_2 = Fe_2SiO_4$; the SG 009 metal, olivine, and orthopyroxene compositions; and assuming a temperature of 1273 K, we calculated $\log fO_2 = -18.2$, which relative to the IW buffer is −3.29, indicating highly reduced formation condition of this material (Fig. 19). This low ΔIW value is similar to the other G chondrites and all are lower than R chondrites, ordinary chondrites, reduced CR chondrites, and even slightly more reduced than the primitive achondrites like the acapulcoites and lodranites (Fig. 19). The juxtaposition of initially oxidizing conditions followed by reducing conditions, even extremely reducing conditions, speaks to the formation of SG 009 chondrules within a chemical microenvironment. Plausible conditions for such microenvironments include collapsing impact vapor plumes within an envelope of hydrogen gas (Stewart et al. 2019).

Large variations in Nb/Ta ratio may also indicate sulfidization. If sulfidization took place, the melt from which silicate chondrules were formed has reacted with vapor or fluid enriched in sulfur. The metal- and

sulfide-enriched mesostases in some chondrules may be evidence of such a process, as well as chalcophile behavior of Nb concentrated in SG 009 sulfides. Possible differentiated precursors of SG 009 silicates could be evaluated with elemental ratios.

Ratios of Zr, Nb, Hf, and Ta should remain constant during volatilization or recondensation. Münker et al. (2003) have shown that different planets are characterized by a wide range in Zr/Hf and Nb/Ta ratio because of the larger incompatibility of Nb relative to Ta and of Zr relative to Hf during partial melting of planetary mantles. In Fig. 20, the Nb/Ta ratios versus Zr/Hf ratios for some of the SG 009 silicates are compared with the Gujba clasts (Oulton et al. 2016) and with planetary basalt compositions from Münker et al. (2003). The SG 009 silicates have Nb/Ta ratios: 3–23, Gujba clasts: 14–21, eucrite: 17–20, Martian meteorites: 13–21, and lunar basalt: 12–23. The Zr/Hf ratios in SG 009 silicates: 22–40, in Gujba clasts: 29–41, eucrite: 34–35, Martian meteorites: 23–34, and lunar basalts: 27–41. While the large range in Nb/Ta ratios represents extreme reduction and sulfidation, the variation in Zr/Hf ratios is likely to reflect processes that affected the precursors to SG 009.

We also observed fractionation of the Th/Sc ratio (0.001–0.006, compared to 0.005 in CI) possibly indicating igneous processing in the chondrule precursors. During evaporation processes, Th and Sc are not fractionated from each other. In contrast, Th is partitioning into melt since it is much more incompatible than Sc. Thus, the SG 009 chondrules may contain a contribution from melting and differentiated crust similar to basalts from the Moon, Mars, and the Earth (Münker et al. 2003). However, given oxygen isotopic compositions between O and E chondrites and the absence of any traces of differentiated clasts, it is difficult to imagine a big differentiated asteroid as a parent body of G chondrites, but we do not exclude such a possibility for the G chondrite initial parent body.

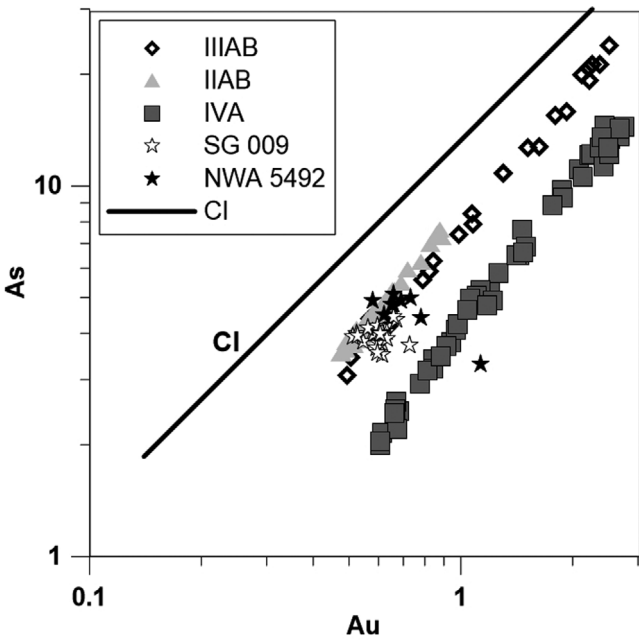

Fig. 16. As versus Au composition of metal phase from SG 009, IIIAB (Wasson 1999), IVA (Wasson and Richardson 2001), IIAB irons (Wasson et al. 2007), and metal phase from NWA 5492 (Weisberg et al. 2015).

Origin of SG 009 and Other G Chondrites

The most important observation distinguishing G chondrites (SG 009, NWA 5492, and GRO 95551) from O, E, and R chondrites is a lack of matrix. The matrix abundance is an important characteristic of all types of chondrites for understanding the origin and evolution of chondrites. Besides G chondrites, no matrix was observed in the ungrouped metal-rich chondrites NWA 12379 and 12273 (Agee et al. 2019; Jansen et al. 2019) nor in metal-rich carbonaceous chondrites, CH-CB groups (Weisberg et al. 1995b). Therefore, our observation shows that chondritic materials with a metal abundance of >20–22% do not contain any fine-grained matrix, only matrix lumps were preserved. Instead of the matrix, all silicate objects are embedded in metal or are surrounded by metal in these meteorites. The cause of this relationship between the abundance of metal and the lack of matrix is not clear. We can only propose that the fine-grained matrix did not survive during the processes of formation of G chondrites and the metal phase was predominant in the region of the G chondrites' formation.

There are other interpretations for the lack of matrix in the metal-rich chondrites. Meibom et al. (2005) reported the FeO-rich composition of the impact in CB chondrites and hypothesized that it may have originally been chondrite matrix that was melted during impact heating. The presence of matrix-like material as dark inclusions (lumps) in the CH and CBb chondrites could be interpreted as clumps of dust that aggregated together with other components and was not dispersed interstitial to the chondrules. However, SG 009 demonstrates minor shock features corresponding to S2 shock stage and it does not contain any traces of impact melt and fine-grained matrix lumps unlike CH and CB chondrites. The lack of matrix could also indicate that the chondrule formation mechanism was more efficient in this region of the disk, because a wide variation in matrix abundances among chondrite groups is observed.

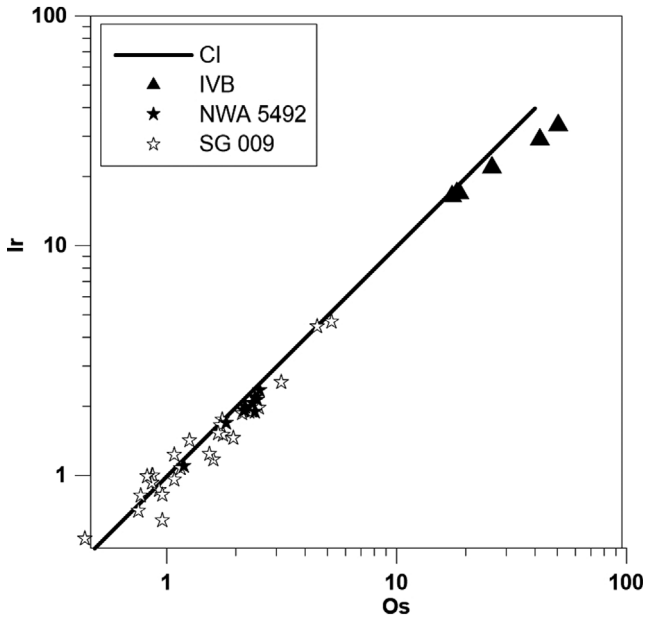

Fig. 17. Ir-Os correlation in metal of SG 009 compared with IVB iron (Campbell and Humayun 2005) and metal of NWA 5492, G-chondrite (Weisberg et al. 2015).

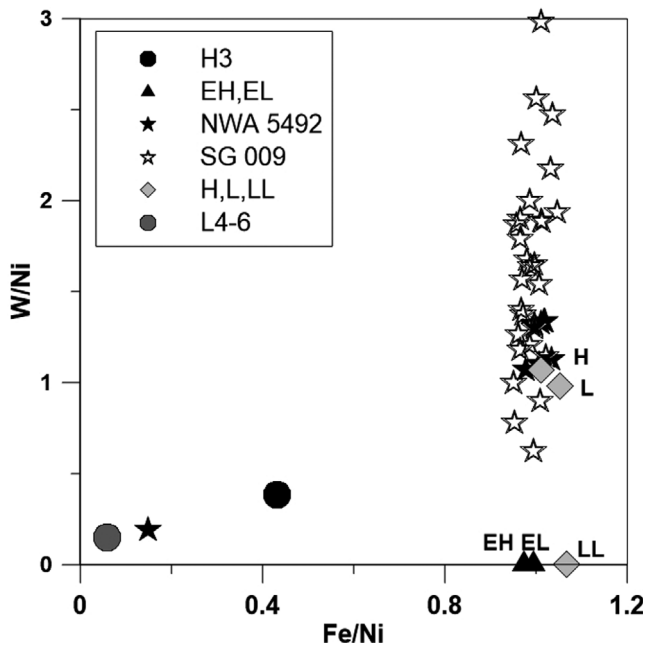

Fig. 18. W/Ni versus Fe/Ni in the SG 009 metal phase. Data are normalized to CI (Anders and Grevesse 1989), and compared to data for metal from OC chondrites (Kong and Ebihara 1997), EH and EL (Kong et al. 1997), and NWA 5492 (Weisberg et al. 2015).

The lack of matrix in the G chondrites may result from similar processes that explain the lack of matrix for CB chondrites but are derived of material from isotopically different oxygen reservoirs. The lack of matrix could indicate a rapid hot accretion as was suggested by Metzler (2012) or formation of G chondrites from an impact vapor plume produced by collision of planetesimals (Stewart et al. 2019). Based on a new physical model for the formation of chondrules and chondrites, mutual collisions between dynamically coexisting planetesimals produce impact vapor plumes that collapse and concentrate a size-sorted mixture of chondrules and dust. The warm cloud of shock-heated gas, dust, and chondrules is a dynamical and thermal anomaly in the nebula with characteristics that assist with new planetesimal formation. Then, condensates from vapor made by impacts between metal- and silicate-rich bodies accreted together (Fedkin et al. 2015). During rapid hot accretion, the dust was evaporated. The young age of chondrules from CB chondrites supports this hypothesis (Krot et al. 2005). If this scenario is accurate, chondrules from G chondrites should also have a young age. Based on metal and silicate geochemistry demonstrating fractionations of trace elements shown above, we can propose that one of the colliding bodies, precursors of G chondrites, might have been partly differentiated.

In the case of the formation of SG 009, unlike other G chondrites, besides the absence of matrix fractionation of silicate and metal compositions, the presence of chromium in the oxidized (Mg-chromite) and sulfide phases (daubréelite and Cr-troilite), graphite veins in Fe,Ni-metal, achondritic clasts, and chondrule-like objects may indicate a mixture of oxidized and reduced, primitive and fractionated material, formed in oxygen isotopic reservoir between O and E chondrites as well as carbon and nitrogen isotopes. Weisberg et al. (2015) noted a close relationship between O, E, R, and G chondrites, which were formed inside the snow line in comparison with C chondrites (Weisberg et al. 2015). However, unlike other G chondrites, SG 009 may preserve traces of oxidizing and reducing material in the final accretion of the G-chondrite parent body.

Thus, G chondrites have unique characteristics and unique processes of their formation resulted in the lack of matrices and enrichment of Fe,Ni-metal phase. The oxygen isotopic compositions plot near the terrestrial fractionation line, a lack of any traces of aqueous alteration, and carbon and nitrogen isotopic evidence of mixing between O and E reservoirs suggest formation of the G chondrites in the inner solar system.

CONCLUSIONS

The meteorites SG 009, North West Africa 5492, and Grosvenor Mountain 95551 represent a new grouplet of metal-rich (>21% of metal) chondrites, the

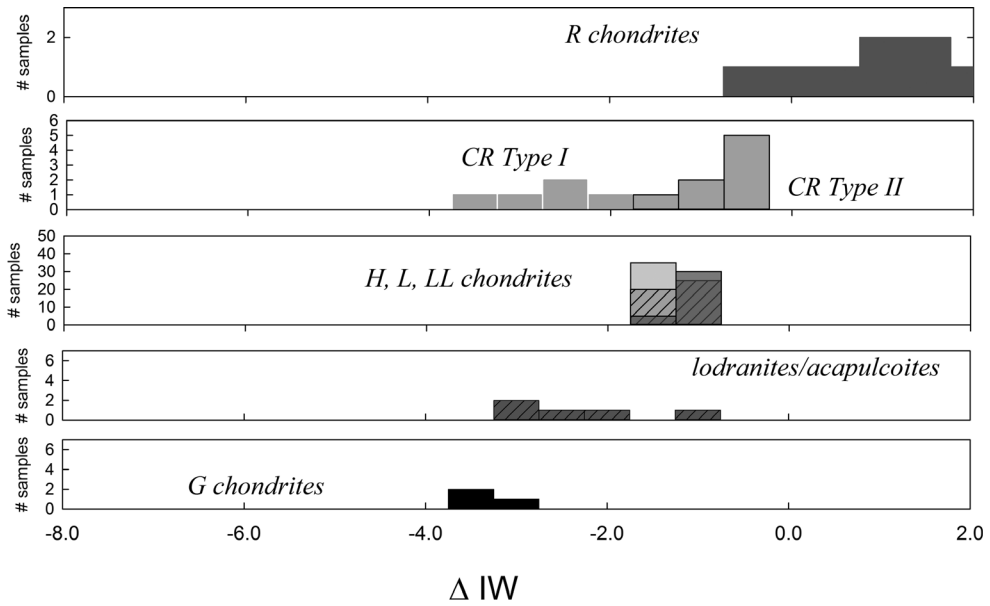

Fig. 19. Histograms of calculated oxygen fugacity (relative to the iron-wüstite buffer or ΔIW) for the G chondrites (Sierra Gorda, GRO 95551, and NWA 5492) compared to R chondrites, Type I and II chondrules in CR chondrites; H, L, and LL chondrites; and lodranites and acapulcoites. The G chondrites are calculated using the equilibrium $Fe + FeSiO_3 + ½ O_2 = Fe_2SiO_4$ (as described by Righter and Drake 1996), mineral compositions from this study, and those reported in Weisberg et al. (2001, 2012, 2015). All other data are from studies cited within Righter et al. (2016).

G chondrites (named from the first member, Grosvenor Mountain 95551), that are not related to CH or CB chondrites based on bulk oxygen, carbon, nitrogen isotopic compositions, mineralogy, and siderophile and lithophile geochemistry. The silicates are very reduced in composition. However, rare oxidized mineral phases occur (Mg-chromite, FeO-rich pyroxene). Sulfides are more abundant in G chondrites than in CH-CB chondrites. SG 009 contains PGE inclusions, unlike NWA 5492 and GRO 95551, that may be connected with oxidation of Fe,Ni-metal or represent remnants of refractory material.

None of the G chondrites contain fine-grained matrix or any matrix lumps enclosing hydrated material similar to matrix lumps in CH-CB chondrites. Average compositions of metal in G chondrites are similar to H chondrite metal, albeit formed in a more reducing environment.

Siderophile and lithophile geochemistry indicates sulfurization during G chondrites formation, and fractionation caused by igneous process of some metal and silicate precursors. The low ΔIW value during SG 009 chondrule formation is similar to the other G chondrites.

Oxygen of all G chondrites shows a range of isotopic compositions. Most have Δ $\Delta^{17}O>0‰$ sandwiched between the bulk enstatite and ordinary chondrites. NWA 5492 and GRO 95551 oxygen

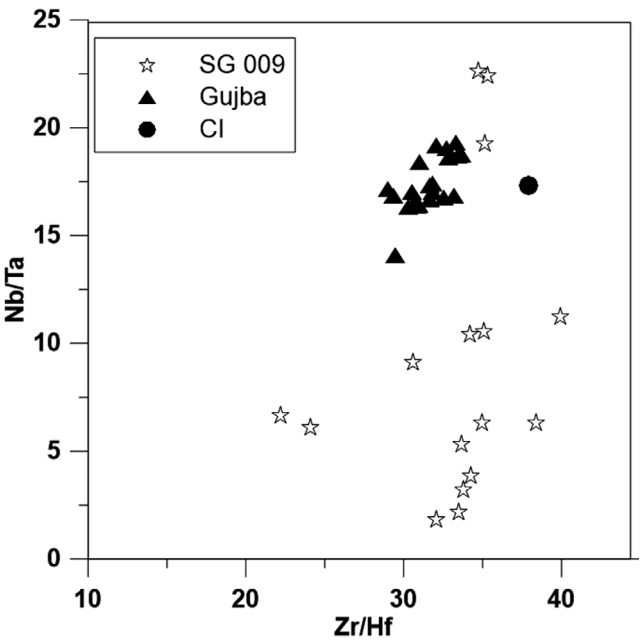

Fig. 20. Nb/Ta versus Zr/Hf for SG 009 silicate chondrules and their fragments, and Gujba CC and BO chondrules (Oulton et al. 2016) relative to chondritic (Anders and Grevesse 1989).

compositions demonstrated a small contribution of R chondrite-like material (Weisberg et al. 2015). An Al-rich chondrule from SG 009 has $\Delta^{17}O>0‰$ that

indicates some heterogeneity in the oxygen isotopic composition of the G chondrite components and contribution of refractory material.

Bulk carbon and nitrogen isotopic compositions of SG 009 correspond to EH and O chondrites. Neon and argon isotopic data reflect a mixture of cosmogenic and solar components. The presence of solar gases suggests exposure to solar wind at the surface of the parent body. The CRE age determined from the concentration of cosmogenic ^{21}Ne is ≥24 Ma, which is typical for O, E, and R chondrites. G chondrites have a relationship with O, E, and R chondrites, and they all represent closely related solar system material (Weisberg et al. 2015). They may represent a unique metal-rich parent asteroid containing both the primitive material and fractionated material from the inner solar system.

The observed oxidizing and reducing conditions during the formation of the SG 009 components indicate a chemical microenvironment. Plausible conditions for such microenvironments, as an example, may include collapsing impact vapor plumes within an envelope of hydrogen gas as a result of collision of planetesimals (Stewart et al. 2019).

Acknowledgments—We thank M. Weisberg, H. Downes, an anonymous reviewer, and Associate Editor C. Goodrich, for their thoughtful reviews which helped to improve this paper. The authors thank Sasha Krot for very fruitful discussions. This work was supported by the Russian Fond of Basic Research no. 20-05-00117A, by Klaus Tschira Stiftung gGmbH, by the NASA Emerging Worlds program (80NSSC18K0595, MH), and we thank the National High Magnetic Field Laboratory, which is supported by National Science Foundation Cooperative Agreement No. DMR-1644779* and the State of Florida. This work was also supported by the Project No. FEUZ-2020-0059 of the Ministry of Science and Higher Education of the Russian Federation. This study was a partial contribution to research theme no. 0137-2019-0002.

Editorial Handling—Dr. Cyrena Goodrich

REFERENCES

Agee C. B., Vaci Z., Ziegler K., and Spilde M. N. 2019. Northwest Africa 12273: Unique ungrouped metal-rich chondrite (abstract #1176). 50th Lunar and Planetary Science Conference. CD-ROM.

Amelin Y. and Krot A. E. 2005. Young Pb-isotopic ages of chondrules in CB carbonaceous chondrites (abstract # 1247). 36th Lunar and Planetary Science Conference. CD-ROM.

Anders E. and Grevesse N. 1989. Abundances of the elements: Meteoritic and solar. *Geochimica et Cosmochimica Acta* 53:197–214.

Bischoff A., Geiger T., Palme H., Spettel B., Schultz L., Scherer P., Loeken T., Bland P., Clayton R. N., Mayeda T. K., Herpers U., Meltzow B., Michel R., and Dittrich-Hannen B. 1994. Acfer 217—A new member of the Rumuruti chondrite group (R) meteorites. *Meteoritics* 29:264–273.

Blum J. D., Wasserburg G. J., Hutcheon I. D., Beckett J. R., and Stolper E. M. 1989. Origin of opaque assemblages in C3V meteorites: Implications for nebular and planetary processes. *Geochimica et Cosmochimica Acta* 53:543.

Campbell A. and Humayun M. 2003. Formation of metal in Grosvenor Mountains 95551 and comparison to ordinary chondrites. *Geochimica et Cosmochimica Acta* 67:2481–2495.

Campbell A. J. and Humayun M. 2005. Composition of the group IVB iron meteorites and their parent melt. *Geochimica et Cosmochimica Acta* 69:4733–4744.

Campbell A. J., Humayun M., Krot A., and Keil K. 2001. Origin of zoned metal grains in the QUE 94411 chondrite. *Geochimica et Cosmochimica Acta* 65:163–180.

Campbell A. J., Humayun M., and Weisberg M. K. 2002. Siderophile element constraints on the formation of metal in the metal-rich chondrites Bencubbin, Gujba and Weatherford. *Geochimica et Cosmochimica Acta* 66:647–660.

Campbell A. J., Humayun M., and Weisberg M. K. 2005. Compositions of unzoned and zoned metal in the CBb chondrites Hammadah al Hamra 237 and Queen Alexandra Range 94627. *Meteoritics & Planetary Science* 40:1131–1148.

Clayton R. N., Mayeda T. K., and Rubin A. E. 1984. Oxygen isotopic compositions of enstatite chondrites and aubrites. Proceedings, 15th Lunar and Planetary Science Conference. *Journal of Geophysical Research* B89:C245–C249.

Clayton R. N., Mayeda T. K., Goswami J. N., and Olsen E. J. 1991. Oxygen isotope studies of ordinary chondrites. *Geochimica et Cosmochim Acta* 55:2317–2337.

Ebel D., Brunner C., Konrad K., Leftwich K., Erb I., Lu M., Rodriguez H., Crapster-Pregont E. J., Friedrich J. M., and Weisberg M. K. 2016. Abundance, major element composition and size of components and matrix in CV, CO and Acfer 094 chondrites. *Geochimica et Cosmochimica Acta* 172:322–356.

Eberhardt P., Eugster O., and Marti K. 1965. A redetermination of the isotopic composition of atmospheric neon. *Zeitschrift für Naturforschung A* 20:623–624.

Eugster O. and Michel T. 1995. Common asteroid break-up events of eucrites, diogenites, and howardites and cosmic-ray production rates for noble gases in achondrites. *Geochimica et Cosmochimica Acta* 59:177–199.

Fedkin A. V., Grossman L., Humayun M., Simon S. B., and Campbell A. J. 2015. Condensates from vapor made by impacts between metal-, silicate-rich bodies: Comparison with metal and chondrules in CB chondrites. *Geochimica et Cosmochimica Acta* 164:236–261.

Friend P., Zipfel J., Gellissen M., Kleinschrod R., Muenker C., Pack A., Schulz T., Stracke A., and Palme H. 2011. Northwest Africa 5492: An extremely reduced chondritic meteorite with low volatile element contents (abstract #1095). 42nd Lunar and Planetary Science Conference. CD-ROM.

Gooding J. L. and Keil K. 1981. Relative abundances of chondrule primary textural types in ordinary chondrites

and their bearing on conditions of chondrule formation. *Meteoritics* 16:17–43.

Grady M. M. and Wright I. P. 2003. Elemental and isotopic abundances of carbon and nitrogen in meteorites. *Space Science Review* 106:231–248.

Heber V. S., Wieler R., Baur H., Olinger C., Friedmann T. A., and Burnett D. S. 2009. Noble gas composition of the solar wind as collected by the Genesis mission. *Geochimica et Cosmochimica Acta* 73:7414–7432.

Hewins R. H., Bourot-Denis M., Zanda B., Leroux H., Barrat J.-A., Humayun M., Göpel C., Greenwood R. C., Franchi I. A., Gattacceca J., Pont S., Lorand J.-P., Rochette P., Kuga M., Marty B., Courne C., and Marrocchi Y. 2014. The Paris meteorite: The least altered CM chondrite so far. *Geochimica et Cosmochimica Acta* 124:190–222.

Humayun M. 2012. Chondrule cooling rates inferred from diffusive profiles in metal lumps the Acfer 097 CR2 chondrite. *Meteoritics & Planetary Science* 47:1191–1208.

Humayun M. and Campbell A. J. 2002. The duration of ordinary chondrite metamorphism inferred from tungsten microdistribution in metal. *Earth and Planetary Science Letters* 198:225–243.

Humayun M., Davis F. A., and Hirschmann M. M. 2010. Major element analysis of natural silicates by laser ablation ICP-MS. *Journal of Analytic Atomic Spectrometry* 25:998–1005.

Ivanova M. A. and Petaev M. I. 2015. Characteristics and origin of the components of the carbonaceous chondrite NWA 470. *Petrology* 23:150–167.

Ivanova M. A., Kononkova N. N., and Nazarov M. A. 2001. Rutile and Mn-rich chromite-bearing sulfide nuggets in an unusual inclusion from the Ghubara L5 chondrite (abstract #1715). 31st Lunar and Planetary Science Conference. CD-ROM.

Ivanova M. A., Kononkova N. N., Krot A. N., Greenwood R. C., Franchi I. A., Verchovsky A. B., Trieloff M., Korochansteva E. V., and Brandstaetter F. 2008. The Isheyevo meteorite: Mineralogy, petrology, bulk chemistry, oxygen, nitrogen, carbon isotopic compositions and ^{40}Ar-^{39}Ar ages. *Meteoritics & Planetary Science* 43:915–940.

Ivanova M. A., Lorenz C. A., Humayun M., Richter K., Corrigan C. M., Franchi I. A., Verchovsky A. B., Korochantseva E. V., Kozlov V. V., Teplyakova S. N., Kononkova N. N., and Korochantsev A. V. 2019. Properties of a new grouplet of G metal-rich chondrites. *Meteoritics & Planetary Science* 54:6143.

Jansen C. A., Brenker F. E., Krot A. N., Zipfel J., Pack A., Labenne L., Bizzarro M., and Schiller M. 2019. Mineralogy, petrology, and oxygen isotopic composition of Northwest Africa (NWA) 12379, a new metal-rich chondrite with affinity to ordinary chondrites (abstract #2741). 50th Lunar and Planetary Science Conference. CD-ROM.

Keil K. 1968. Mineralogical and chemical relationships among enstatite chondrites. *Journal Geophysical Research* 73:6945–6976.

Kimura M., El Goresy A., Palme H., and Zinner E. 1993. Ca-Al-rich inclusions in the unique chondrite ALH 85085—Petrology, chemistry, and isotopic compositions. *Geochimica et Cosmochimica Acta* 57:2329–2359.

Kita N. T., Nagahara H., Tachibana S., Tomomura S., Spicuzza M. J., Fournelle J. H., and Valley J. W. 2010. High precision SIMS oxygen three isotope study of chondrules in LL3 chondrites: Role of ambient gas during chondrule formation. *Geochimica et Cosmochimica Acta* 74:6610–6635.

Kong P. and Ebihara M. 1997. The origin and nebular history of the metal phase of ordinary chondrites. *Geochimica et Cosmochimica Acta* 61: 2317–2329.

Kong P., Mori T., and Ebihara M. 1997. Compositional continuity of enstatite chondrites and implications for heterogeneous accretion of the enstatite chondrite parent body. *Geochimica et Cosmochimica Acta* 61:4895–4914.

Kong P., Ebihara M., and Palme H. 1999. Distribution of siderophile elements in CR chondrites: Evidence for evaporation and recondensation during chondrule formation. *Geochimica et Cosmochimica Acta* 63:2637–4914.

Korochantseva E. V., Trieloff M., Buikin A. I., Hopp J., and Meyer H.-P. 2005. ^{40}Ar/^{39}Ar dating and cosmic-ray exposure time of desert meteorites: Dhofar 300 and Dhofar 007 eucrites and anomalous achondrite NWA 011. *Meteoritics & Planetary Science* 40:1433–1454.

Krot A. N., Meibom A., Weisberg M. K., and Keil K. 2002. The CR chondrite clan: Implications for early solar system processes. *Meteoritics & Planetary Science* 37:1451–1490.

Krot A. N., Amelin Y., Cassen P., and Meibom A. 2005. Young chondrules in CB chondrites from a giant impact in the early solar system. *Nature* 436:989–992.

Krot A. N., Nagashima K., Bizzarro M., Huss G. R., Davis A. M., McKeegan K. D., Meyer B. S., and Ulyanov A. A. 2008. Multiple generations of refractory inclusions in the metal rich carbonaceous chondrites Acfer 182/214 and Isheyevo. *Astrophysical Journal*. 672:713–721.

Krot A. N., Nagashima K., Yoshitake M., and Yurimoto H. 2010. Oxygen isotope compositions of chondrules from the metal-rich chondrites Isheyevo (CH/CB$_b$), MAC 02675 (CB$_b$) and QUE 94627 (CB$_b$). *Geochimica et Cosmochimica Acta* 74:2190–2211.

Krot A. N., Nagashima K., and Petaev M. I. 2012. Isotopically uniform, ^{16}O-depleted calcium, aluminum-rich inclusions in CH and CB carbonaceous chondrites. *Geochimica et Cosmochimica Acta* 83:159–178.

Krot A. N., Keil K., Goodrich C., Weisberg M. K., and Scott E. R. D. 2014. Classification of meteorites. In *Meteorites and cosmochemical processes*, Vol. 1 Treatise on geochemistry, 2nd ed., edited by Davis A. M. Oxford: Elsevier. pp. 1–63.

Krot A. N., Nagashima K., van Kooten E. M. M., and Bizzarro M. 2017. High-temperature rims around calcium-aluminum-rich inclusions from the CR, CB and CH carbonaceous chondrites. *Geochimica et Cosmochimica Acta* 201:155–184.

Leya I. and Masarik J. 2009. Cosmogenic nuclides in stony meteorites revisited. *Meteoritics & Planetary Science* 44:1061–1086.

Maruyama S., Yurimoto H., and Sueno S. 1999. Oxygen isotope evidence regarding the formation of spinel-bearing chondrules. *Earth and Planetary Science Letter* 169:165–171.

Meibom A., Petaev M. I., Krot A. N., Wood J. A., and Keil K. 1999. Primitive FeNi metal grains in CH carbonaceous chondrites formed by condensation from a gas of solar composition. *Journal of Geophysical Research*. 104:22,053–22,059.

Meibom A., Righter K., Chabot N., Dehn G., Antignano A., McCoy T. J., Krot A. N., Zolensky M. E., Petaev M. I., and Keil K. 2005. Shock melts in QUE 94411,

Hammadah al Hamra 237, and Bencubbin: Remains of the missing matrix? *Meteoritics & Planetary Sciences* 40:1377–1391.
Metzler K. 2012. Ultra rapid chondrite formation by hot accretion? Evidence from ordinary chondrites. *Meteoritics & Planetary Sciences* 47:2193–2217.
Miller M. F., Franchi I. A., and Pillinger C. T. 1999. High precision measurements of the oxygen isotope mass-depended fractionation line for the Earth-Moon system (abstract #1729). 30th Lunar and Planetary Science Conference. CD-ROM.
Münker C., Pfander J. A., Weyer S., Buchl A., Klein T., and Mezger K. 2003. Evolution of planetary cores and the Earth-Moon system from Nb/Ta systematics. *Science* 301:84–87.
Newsom H. E., and Drake M. J. 1979. The origin of metal clasts in the Bencubbin meteorite breccia. *Geochimica et Cosmochimica Acta* 43:689–707.
Ott U. 2002. Noble gases in meteorites—Trapped components. In *Noble gases*, edited by Porcelli D. P., Ballentine C. J., and Wieler R. P. *Reviews in Mineralogy and Geochemistry* 47: 71–100.
Oulton J., Humayun M., Fedkin A., and Grossman L. 2016. Chemical evidence for differentiation, evaporation and recondensation from silicate clasts in Gujba. *Geochimica et Cosmochimica Acta* 177:254–274.
Righter K. and Drake M. 1996. Core formation in Earth's Moon, Mars, and Vesta. *Icarus* 124:513–529.
Righter K., Sutton S. R., Danielson L., Pando K., and Newville M. 2016. Redox variations in the inner solar system with new constraints from vanadium XANES in spinels. *American Mineralogist* 101:1928–1942.
Rubin A. E. 2004. Postshock annealing and postannealing shock in equilibrated ordinary chondrites: Implications for the thermal and shock histories of chondritic asteroids. *Geochimica et Cosmochimica Acta* 68:678–689.
Rubin A. E. 2010. Physical properties of chondrules in different chondrites groups: Implications for multiple melting events in dusty environments. *Geochimica et Cosmochimica Acta* 74:4807–4828.
Rubin A. E., Kallemeyn G. W., Wasson J. T., Clayton R. N., Mayeda T. K., Grady M., Verchovsky A. B., Eugster O., and Lorenzetti S. 2003. Formation of metal and silicate globules in Gujba: A new Bencubbin-like meteorite fall. *Geochimica et Cosmochimica Acta* 67:3283–3298.
Russell S. S., McCoy T. J., Jerosewich E., and Ash R. D. 1998. The Burnwell, Kentucky, low iron oxide chondrite fall. *Meteoritics & Planetary Science* 33:853–856.
Schulze H. 2007. Mineralogy and mineral chemistry of noble metal grains in R chondrites (abstract #1720). 30th Lunar and Planatary Science Conference. CD-ROM.
Stewart S. T., Carter P. J., Davies E. J., Lock S. J., Kraus R. G., Root S., Petaev M. I., and Jacobsen S. B. 2019. Collapsing impact vapor plume model for chondrule and chondrite formation (abstract #1251). 50th Lunar and Planetary Science Conference. CD-ROM.
Stoffler D., Keil K., and Scott E. R. D. 1991. Shock metamorphism of ordinary chondrites. *Geochimica et Cosmochimica Acta* 55:3845–3867.
Sugiura N., Zashu S., Weisberg M. K., and Prinz M. 2000. A nitrogen isotope study of bencubbinites. *Meteoritics & Planetary Science* 35:987–996.
Teplyakova S. N., Humayun M., Lorez C. A., and Ivanova M. A. 2012. A common parent for IIE iron meteorites and H chondrites (abstract #1130). 43rd Lunar and Planetary Science Conference. CD-ROM.
Troiano J., Rumble D. III, Abd Rivers M. L., and Friedrich J. M. 2011. Composition of three low- FeO ordinary chondrites: Indicators of common origin with the H chondrites. *Geochimica et Cosmochimica Acta* 75:6511–6519.
Van Niekirk D., Keil K., and Humayun M. 2014. Petrogenesis of anomalous Queen Alexandra Range enstatite meteorites and their relation to enstatite chondrites, primitive enstatite achondrites, and aubrites. *Meteoritics & Planetary Science* 49:295–312.
Verchovsky A. B. 2017. Origin of isotopically light nitrogen in meteorites. *Geochemistry International* 55:957–970.
Verchovsky A. B., Fisenko A. V., Semjonova L. F., Wright I. P., Lee M. R., and Pillinger C. T. 1998. C, N, and noble gas isotopes in grain size separates of presolar diamonds from Efremovka. *Science* 281:1165.
Verchovsky A. B., Sephton M. A., Wright I. P., and Pillinger C. T. 2002. Separation of planetary noble gas carrier from bulk carbon in enstatite chondrites during stepped combustion. *Earth and Planetary Science Letters* 199:243–255.
Wang J., Davis A. M., Clayton R. N., Mayeda T. K., and Hashimoto A. 2001. Chemical and isotopic fractionation during the evaporation of the FeO-MgO-SiO 2-CaO-Al 2O 3-TiO 2 rare earth element melt system. *Geochimica et Cosmochimica Acta* 65:479-494.
Wasson J. T. 1999. Trapped melt in IIIAB irons; solid/liquid elemental partitioning during the fractionation of the IIIAB Magma. *Geochimica et Cosmochimica Acta* 63:2875–2889.
Wasson J. T. and Kallemeyn G. W. 1990. Allan Hills 85085: A subchondritic meteorite of mixed nebular and regolithic heritage. *Earth and Planetary Science Letter* 101:148–161.
Wasson J. T. and Richardson J. W. 2001. Fractionation trends among iva iron meteorites: Contrasts with IIIAB trends. *Geochimica et Cosmochimica Acta* 65:951–970.
Wasson J. T., Huber H., and Malvin D. J. 2007. Formation of IIAB iron meteorites. *Geochimica et Cosmochimica Acta* 71:760–781.
Weber D., Zinner E., and Bischoff A. 1995. Trace element abundances and magnesium, calcium, and titanium isotopic compositions of grossite-containing inclusions from the carbonaceous chondrite Acfer 182. *Geochimica et Cosmochimica Acta* 59:803–823.
Weber H. W., Frank L., and Schultz L. 2001. Subsolar noble gases in metal-rich carbonaceous (CH) chondrites. *Meteoritics & Planetary Science* 36:A220.
Weisberg M. K., Prinz M., and Nehru C. E. 1990. The Bencubbin chondrite breccia and its relationship to CR chondrites and the ALH85085 chondrite. *Meteoritics* 25:269–279.
Weisberg M. K., Bosenberg J. S., Kozhusko G., Prinz M., Clayton R. N., and Mayeda T. K. 1995a. EH3 and EL3 chondrites: A petrologic-oxygen isotopic study (abstract #1481). 26th Lunar and Planetary Science Conference. CD-ROM.
Weisberg M. K., Prinz M., Clayton R. N., Mayeda T. K., Grady M. M., and Pillinger C. T. 1995b. The CR chondrite clan. *Proceedings of NIPR Symposium on Antarctic Meteorites* 8:11–32.
Weisberg M. K., Prinz M., Clayton R. N., Mayeda T. K., Sugiura N., Zashu S., and Ebihara M. 2001. A new metal-

rich chondrite grouplet. *Meteoritics & Planetary Science* 36:401–418.
Weisberg M. K., Bunch T. E., Wittke J. H., Rumble D. III, and Ebel D. S. 2012. Petrology and oxygen isotopes of NWA 5492, a new metal-rich chondrite. *Meteoritics & Planetary Science* 47:363–373.
Weisberg M. K., Ebel D. S., Nakashima D., Kita N. T., and Humayun M. 2015. Petrology and geochemistry of chondrules and metal in NWA 5492 and GRO 95551: A new type of metal-rich chondrite. *Geochimica et Cosmochimica Acta* 167:269–285.
Wright I. P. and Pillinger C. T. 1989. Carbon isotopic analysis of small samples by use of stepped-heating extraction and static mass spectrometry. *U.S. Geological Bulletin* 7890:9–34.
Wieler R. 2002. Cosmic-ray-produced noble gases in meteorites. In *Noble gases*, edited by D. P. Porcelli, C. J. Ballentine, and R. P. Wieler. *Reviews in Mineralogy and Geochemistry* 47:125–170.
Wright I. P., Boyd S. R., Franchi I. A., and Pillinger C. T. 1988. High-precision determination of nitrogen stable isotope ratios at the sub-nanomole level. *Journal of Physics* E 21: 865–875.

SUPPORTING INFORMATION

Additional supporting information may be found in the online version of this article.

Fig. S1. BSE image of the SG 009 section with data points analyzed by LA-ICP-MS method of (a) metal and silicates, (b) silicates and sulfides.

Fig. S2. (a) BSE image of the sample showing the regions G1, G9, G18, and the location of the single SIMS analysis "OL" (olivine), SP (spinel), PX (pyroxene). (b), (c), and (d) are overlays of EDX mappings (red = Mg, green = Ca, blue = Al,) and reflected light images of regions G1, G9, and G18. The reflected light images were taken while the sample was still coated with gold. The dark squares in the reflected light images are the SIMS spots.